Plasma Sources Science and Technology

PAPER • **OPEN ACCESS**

Charged particle kinetics and gas heating in CO_2 microwave plasma contraction: comparisons of simulations and experiments

To cite this article: L Vialetto *et al* 2022 *Plasma Sources Sci. Technol.* **31** 055005

OPEN ACCESS
IOP Publishing
Plasma Sources Science and Technology
Plasma Sources Sci. Technol. **31** (2022) 055005 (24pp)
https://doi.org/10.1088/1361-6595/ac56c5

Charged particle kinetics and gas heating in CO_2 microwave plasma contraction: comparisons of simulations and experiments

L Vialetto[1,2,*], A W van de Steeg[1], P Viegas[1,3], S Longo[4], G J van Rooij[1,5], M C M van de Sanden[1,2], J van Dijk[2] and P Diomede[5]

[1] DIFFER—Dutch Institute for Fundamental Energy Research, De Zaale 20, 5612 AJ Eindhoven, The Netherlands
[2] Department of Applied Physics, Eindhoven University of Technology, PO Box 513, 5600 MB Eindhoven, The Netherlands
[3] Department of Physical Electronics, Faculty of Science, Masaryk University, 611 37 Brno, Czech Republic
[4] Dipartimento di Chimica, Università degli Studi di Bari, via Orabona 4, 70126 Bari, Italy
[5] Faculty of Science and Engineering, Maastricht University, Paul Henri Spaaklaan 1, 6229 GS Maastricht, The Netherlands

E-mail: l.vialetto@tue.nl

Received 9 December 2021, revised 2 February 2022
Accepted for publication 18 February 2022
Published 12 May 2022

Abstract

This work investigates kinetics and transport of CO_2 microwave plasmas through simulation results from a 1D radial fluid model and experiments. Simulation results are validated against spatially resolved measurements of neutral species mole fractions, gas temperature, electron number density and temperature obtained by means of Thomson and Raman scattering diagnostics, yielding good agreement. As such, the model is used to complement experiments and assess the main chemical reactions, mass and energy transport in diffuse and contracted plasma regimes. From model results, it is found that, as pressure is raised, the inhomogeneous gas heating induces significant gradients in neutral and charged species mole fractions profiles. Moreover, the transition from diffuse to contracted plasma is accompanied by a change in the dominant charged species, which favours electron–ion recombination over dissociative attachment. Associative ionization rates increase in the plasma core from diffuse to contracted regime. These processes contribute to the increase in the peak electron number density with pressure, that determines radial plasma contraction.

Keywords: carbon dioxide conversion, fluid model, microwave plasma, discharge contraction

(Some figures may appear in colour only in the online journal)

1. Introduction

In the past few years, a lot of attention has been devoted to the study of CO_2 dissociation by means of microwave (MW) discharges [1–5]. Most of this work has been motivated by high energy efficiencies, up to 80%, that have been reported

* Author to whom any correspondence should be addressed.

in experimental investigations with subsonic vortex-confined MW reactors by former Soviet Union scientists [6–9]. These high energy efficiencies have been mainly explained by preferential mechanisms leading to the onset of non-equilibrium between vibrational and translational degrees of freedom of the CO_2 molecules, favouring CO_2 dissociation at low gas temperatures. Despite numerous efforts by researchers around the world, these high energy efficiencies have never been reproduced. In fact, in plasma-assisted CO_2 conversion there is an increasingly complicated interplay of many effects, namely transport of reactive flows, complex chemistry with several species and electromagnetic fields. The interplay of these effects is not well known, but it is yet important for optimization of the reactor performances [10].

Advanced laser scattering diagnostics have been employed to obtain *in situ* measurements of rotational and vibrational temperatures in CO_2 MW discharges [11–13]. It has been observed that non-equilibrium between different modes of vibration of the CO_2 molecule can be obtained by modulation of the MW power. Nevertheless, these studies suggest that, in both pulsed and continuous-wave (CW) experiments, CO_2 dissociation does not preferentially exploits non-equilibrium effects, but rather the high gas temperature in the plasma core, ranging from 3000 K to 7000 K [14–16]. In these conditions, the complex chemistry of CO_2 MW plasmas is typically studied by means of 0D models [17–21]. In particular, the study by Pietanza *et al* [22] suggests that CO and O can be described by a thermodynamic approach, while other minority species present large deviations from thermodynamic equilibrium. Similarly, in the work by Viegas *et al* [23], a chemical kinetics scheme for the study of CO_2 dissociation in MW discharges at intermediate to high pressures (from 60 mbar to 300 mbar) has been proposed. In [23], it has been observed that mass transport is fundamental to describe the composition in the core of a vortex-stabilized MW reactor [14]. It is generally found that 0D models can qualitatively explain the behaviour of the discharge core, but discrepancies between calculations and recent experimental measurements are still present. For example, calculations by Pietanza *et al* [22] at 100 mbar and 250 mbar predict a neutral species composition that is largely different than the one obtained by means of Raman scattering [10, 24], with C-atom mole fractions higher than in the measurements. Moreover, for the same MW input power, both models in [22, 23] predict an increase in the electron temperature with increasing pressure, that is in contrast with recent experimental measurements obtained via Thomson scattering at DIFFER [25]. These discrepancies suggest that further studies are needed to accurately describe the main electron-related properties of the discharge, such as electron temperature and electron number density. Indeed, chemical kinetics schemes employed in these models have not been extensively validated against experimental measurements of discharge parameters, such as neutral and charged species mole fractions, electron and gas temperatures. This is mainly due to the lack of data or to strong assumptions that are implicit in 0D model calculations that limit the applicability of these models to spatially homogeneous conditions.

In order to describe the spatial inhomogeneities of discharge parameters in CO_2 discharges, 1D or 2D fluid models are typically employed. For example, Kotov and Koelman [26] developed a 1D steady-state axial plug flow model for a MW plasma reactor. Nevertheless, the chemistry set used in [26] has been originally employed for studies of dielectric-barrier discharges (DBDs) [19] and not for MW discharges, that typically exhibit very different power densities and gas temperatures. A similar reaction scheme has been used by Ponduri *et al* [27] and by Wang *et al* [28] in a 1D axial fluid model to study CO_2 dissociation in a geometrically symmetric DBD and in a gliding arc (GA) discharge. In particular, in [28], it has been found that CO_2 dissociation in GA discharges occurs mainly through collisions with oxygen atoms and exploiting the non-equilibrium vibrational distribution function (VDF) of CO_2 molecules. However, a detailed validation of that model has not been performed due to the lack of experimental data for GA plasmas in literature. CO_2 dissociation in MW plasmas has been studied by Sun *et al* [29] by means of a 1D axial fluid model. They found that there is little difference between gas, vibrational and electron temperatures in the plasma, thus CO_2 dissociation in MW discharges is mostly driven by thermal chemistry. The same conclusions about thermal dissociation in CO_2 MW plasmas have been drawn by Wolf *et al* [30], where a 2D fluid model of the reactor used at DIFFER has been employed. However, the model developed by Wolf *et al* [30] considers the plasma simply as a heat source. Hence, it neglects the role of charged particle kinetics on CO_2 dissociation and on the radial contraction of the plasma taking place between moderate and atmospheric pressures.

The discharge contraction plays an important role in CO_2 conversion. In fact, the optimal condition for CO_2 conversion is achieved concurrently with this phenomenon [15, 16]. The mechanisms triggering contraction in molecular plasmas are not fully understood and spatially-resolved (fluid) models are important tools to shed light on them. Specifically, based on recent studies on atomic plasmas, two different mechanisms have been identified as responsible for plasma contraction: (i) electron–electron collisions, or (ii) non-uniform gas heating along the tube radius. The role of electron–electron collisions has been investigated by Golubovskii *et al* [31] and by Petrov and Ferreira [32], with the conclusion that these collisions have an important influence on the electron energy distribution function (EEDF) and, in turn, on increasing electron impact ionization rate coefficients in the plasma core and not on the edges. The non-uniform gas heating along the discharge radius has been considered by Martinez *et al* [33], by Ridenti *et al* [34], and by Moisan and Pellettier [35] as the main mechanism driving contraction in Ar, Ne and N_2 MW plasmas. In particular, in [33], it has been hypothesized that radial gradients of gas temperature have an influence on the reduced electric field and on decreasing charged particle losses through dissociative recombination in the core where atomic ions emerge, but not on the edges. Nevertheless, a satisfactory interpretation of the contraction phenomenon in CO_2 MW plasmas is still lacking since, in particular, plasma chemistry models employed so far have not been extensively validated against experiments.

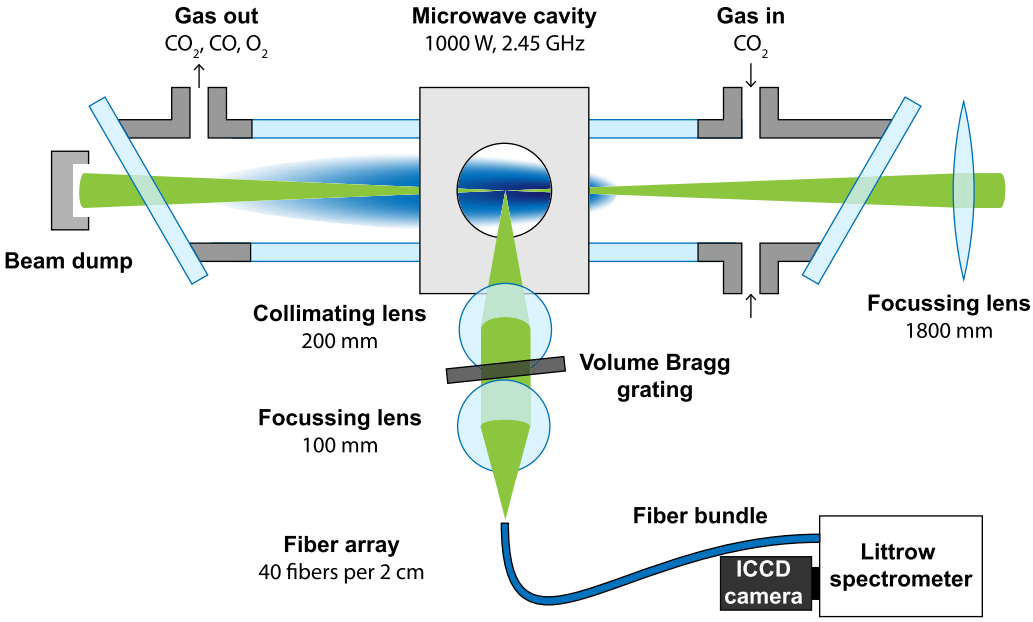

Figure 1. Schematic of the combined MW plasma and laser scattering setup [24]. Reprinted with permission from [25]. Copyright (2022) American Chemical Society.

In this work, a 1D radial fluid model is developed to study the contraction of CO_2 MW discharges. Moreover, results of the model are validated against spatially-resolved measurements of the main neutral species mole fractions, electron number density, gas and electron temperatures obtained by means of laser scattering diagnostics. The present study aims at extending the detailed investigation by Viegas *et al* [23], where a 0D plasma chemistry model has been developed for the study of contraction in CO_2 MW plasmas. In this work, the radial profiles of the aforementioned quantities and their relation with discharge contraction are investigated.

The paper is organized as follows. Section 2 summarizes the experimental conditions considered in this work. Section 3 presents a 1D radial fluid model coupled with a Monte Carlo flux (MCF) code for electron kinetics [36, 37], with particular emphasis on the assumptions and input parameters that have been used in the model. Results of the model are compared with experimental measurements of the main neutral species mole fractions and gas temperature in subsection 4.1, and with electron number density and temperature in subsection 4.2, for a MW discharge operated at 700 W and 1000 W input MW power, 10 slm gas flow rate, and pressures from 100 mbar to 400 mbar. Insights into CO_2 MW plasma contraction are illustrated in subsection 4.3. Subsection 4.4 investigates the effect of uncertainties in parameters, such as the input MW power density and chemical rate coefficients, on the model results. Conclusions and perspectives for future work are illustrated in section 5.

2. Experimental conditions

Figure 1 shows a schematic of the setup in which experimental data are acquired. The experimental setup has been described in detail by Wolf *et al* [14, 15], Viegas *et al* [23], and van de Steeg *et al* [24] and it consists of a vortex-stabilized MW reactor, with a 2.45 GHz MW source combined with laser scattering diagnostics. A pure CO_2 gas is injected tangentially into a quartz tube of 27 mm inner diameter that is placed inside a MW cavity consisting of rectangular waveguides. Gas flow rates (Φ) of 10 slm and pressures (p_g) in the range 100–400 mbar are considered in this work. MWs are supplied to the system by a magnetron operating at 700 W or 1000 W input power. The impedance of the system is optimized to minimize reflected power. The laser diagnostics allows one for simultaneous and spatially resolved measurements of rotational (gas) and electron temperatures as well as mole fractions of CO_2, CO, O_2, and O, and electron number densities [24, 25].

Figure 2 shows the intensity distribution of the 777 nm spectral line emission of atomic oxygen ($O(3p\,^5P) \rightarrow O(3s\,^5S)$) recorded for a CO_2 MW plasma at 100 mbar and 250 mbar, a gas flow rate of 10 slm and MW input power of 1000 W.

In particular, a broad intensity distribution in the radial and axial directions has been recorded at 100 mbar, that is typical of a diffuse plasma regime, whereas, at 250 mbar, the intensity distribution is narrower in the radial direction and more elongated in the axial direction, that is typical of a contracted plasma regime [15]. The relation between intensity distribution and electron density profile in CO_2 MW plasmas has been investigated by Viegas *et al* [38].

In this work, two different sets of input parameters for the model are considered. The two sets of data are acquired from the same experimental setup that is shown in figure 1. The first set is summarized in table 1 and it is used for comparison of model results with measurements of neutral species mole fractions and gas temperature obtained with spontaneous Raman scattering. The application of Raman scattering is described in [24] and these conditions correspond to a total input MW power of 700 W.

Table 1. Overview of input parameters used in the fluid model for a CO_2 MW discharge at a total input MW power of 700 W. The values of the parameters have been obtained by the experiment described in [24].

p_g (mbar)	$P_{in}(0)$ (W m^{-3})	W (mm)	L (mm)
100	2.02×10^9	6.99	24
150	6.16×10^9	2.26	29

Table 2. Overview of input parameters used in the fluid model for a CO_2 MW discharge at a total input MW power of 1000 W. The values of the parameters have been obtained by the experiment described in [25].

p_g (mbar)	$P_{in}(0)$ (W m^{-3})	W (mm)	L (mm)
100	1.88×10^9	6.45	19
150	6.17×10^9	2.43	22
200	5.61×10^9	2.38	23
250	5.57×10^9	2.28	24
300	5.29×10^9	2.26	26
400	4.69×10^9	2.19	27

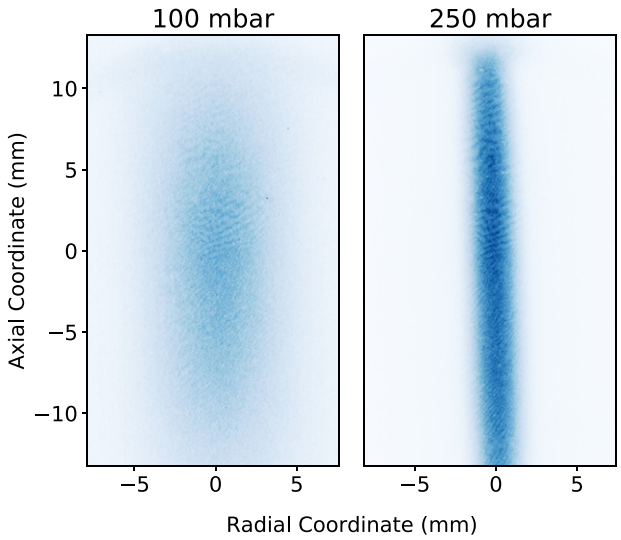

Figure 2. Visual appearance of CO_2 MW plasma detected using a Charged-Coupled Device (CCD) camera in diffuse (left) and contracted (right) regime, at 100 mbar and 250 mbar, respectively.

Specifically, the peak power density at the plasma center ($P_{in}(0)$) has been obtained by normalization of the emission intensity profile to the total input MW power [14]. The assumptions underlying this derivation are discussed by Viegas *et al* [38]. The width of power density profile (W) and the length of the plasma (L) are defined as the full-width at half maximum (FWHM) of the spontaneous emission intensity profiles of the atomic oxygen triplet lines in radial and axial direction, respectively [14].

The second set of input parameters is summarized in table 2 and is used for the comparison of model results with measurements of electron number density and electron temperature obtained with Thomson scattering. The use of Thomson scattering is described in the work by van de Steeg *et al* [25] and this set corresponds to a total input MW power of 1000 W.

The reason behind the use of two different sets of input parameters, one for 700 W (table 1) and the other for 1000 W (table 2), is twofold. First, at 1000 W, the Raman signature in the spectra gets perturbed by the presence of C_2 emission [24, 39], while the same emission has not been recorded for the 700 W conditions. Second, at 1000 W, the Thomson signal can still be fitted over the C_2 emission. Moreover, the 1000 W case is preferred over the 700 W for Thomson scattering measurements also because of the higher electron number density peak that is obtained as a result of the higher deposited MW power density. As discussed in subsection 4.1, by validating neutral species mole fractions and gas temperature for the first set of conditions, we consider the model to accurately reproduce these quantities also for the second set of conditions.

3. Model

A novel 1D radial fluid model for CO_2 MW plasmas has been developed. Due to interactions with other neutrals and charged species, CO_2 molecules dissociate into the plasma giving rise to a multi-component mixture of species. In this respect, the model solves a system of coupled mass balance equations for neutral (CO_2, CO, O, O_2, C) and charged species (CO_2^+, CO^+, O^+, O_2^+, C^+, O^-, and e), and an equation for the gas temperature (T_g). The fluid model is coupled to a MCF solver for the electron Boltzmann equation [36, 37] that provides the reduced electric field (E/n) and electron properties of the discharge, such as electron impact rate coefficients, electron transport parameters, electron temperature (T_e). The coupling is discussed in the following subsections. One of the main assumptions considered in this work is that only variations of discharge parameters in the radial direction of the discharge vessel are taken into account. Moreover, the system is considered at steady-state, as in experiments. The importance of radial mass and energy transport for the description of CO_2 dissociation in the DIFFER reactor has been highlighted by Wolf *et al* [30], where a 2D fluid model has been used to model CO_2 reactive gas flows. Furthermore, note that axial transport is not completely neglected in the present model and the effect of axial gas flow is taken into account as a source/loss term for the mass and energy balance equations. The experimental parameters in tables 1 and 2 are used as input for the model. The calculated species mole fractions, gas and electron temperature are validated against spatially-resolved measurements performed at DIFFER. The model is also used to complement experiments, by providing calculations of charged species mole fractions that are not directly measured.

3.1. Mass balance equations

The mass conservation equation involves the total number density n and mass density ρ of the mixture that are defined as

$$n = \sum_i n_i, \tag{1}$$

$$\rho = \sum_i \rho_i = \sum_i m_i n_i, \tag{2}$$

where m_i, n_i, and ρ_i are the mass, number density and mass density of the ith species, respectively [40]. From equations (1) and (2), the species mole fraction x_i and the species mass fraction y_i are defined as

$$x_i = \frac{n_i}{n}, \qquad y_i = \frac{\rho_i}{\rho}. \tag{3}$$

Moreover, in a multi-component reactive mixture, the mixture mass can be defined as

$$m = \sum_i m_i x_i. \tag{4}$$

In 1D cylindrical coordinates, the mass balance equation for the ith species in the mixture is expressed as

$$\frac{1}{r}\frac{\mathrm{d}}{\mathrm{d}r}(rJ_i) = m_i\omega_i + \Omega_i, \tag{5}$$

with J_i the diffusive mass flux of species i, ω_i the production rate of species i due to chemical reactions, and Ω_i accounts for the transport of species due to convective axial flow. The species production rate is calculated from

$$\omega_i = \sum_j \nu_{ji} R_j, \tag{6}$$

with ν_{ij} the stoichiometric coefficient, and R_j the reaction rate for the jth chemical process.

The effect of axial gas flow is accounted for as a source term in the right-hand side of equation (5) representing the inflow of CO_2 as

$$\Omega_{i=\mathrm{CO_2}} = \rho\left(1 - y_{\mathrm{CO_2}}\right)\frac{v_{\mathrm{axial}}}{L}, \tag{7}$$

where L is the plasma length that is estimated from measurements the emissivity profile of the 777 nm spectral line emission of atomic oxygen ($O(3p^5P) \rightarrow O(3s^5S)$), and v_{axial} is the axial speed of the inflow gas defined from the conservation of the mass flow rate as

$$v_{\mathrm{axial}} = \frac{1}{S_{\mathrm{tube}}}\frac{\dot{m}}{\sum_i \rho_i}, \tag{8}$$

where S_{tube} is the cross sectional area of the tube and $\dot{m} = \rho_{\mathrm{env}}\Phi$ is the input mass flow rate, with Φ the input gas flow rate and ρ_{env} the environment mass density that is composed by CO_2 at 300 K. Similarly, the outflow for the ith species, other than CO_2, at the end of the reactor is given by

$$\Omega_{i\neq\mathrm{CO_2}} = -\rho y_i \frac{v_{\mathrm{axial}}}{L}. \tag{9}$$

Note that equations (7)–(9) are defined such that the continuity equation for the mixture as a whole is satisfied. Indeed, the same approach has been adopted by Viegas *et al* [23, 38] in order to take into account gas flow effects in 0D and 1D model calculations.

The mass flux J_i for the ith species [41, 42] is

$$J_i = \rho\left[\frac{q_i}{|q_i|}y_i\mu_i E_{\mathrm{amb}} - D_i\left(\frac{\mathrm{d}y_i}{\mathrm{d}r} + \frac{y_i}{m}\frac{\mathrm{d}m}{\mathrm{d}r} - \frac{k_i^{\mathrm{T}}}{T_{\mathrm{g}}}\frac{m_i}{m}\frac{\mathrm{d}T_{\mathrm{g}}}{\mathrm{d}r}\right)\right], \tag{10}$$

where q_i is the charge of species i, μ_i is the mobility of species i in the mixture, E_{amb} is the ambipolar electric field in the radial direction due to radial charge separation, D_i is an effective diffusion coefficient for species i in a multi-component mixture. Note that three contributions are included for the radial diffusion, that are (i) gradients of mole fractions, (ii) gradients in mixture mass, and (iii) thermophoretic forces, where the expressions for the thermal diffusion ratio k_i^{T} of the ith species are taken from the work by Fristom and Monchick [43]. The mass diffusion of species i in a multi-component mixture is described by means of a diffusion coefficient

$$D_i = D_i^{\mathrm{M}} + D_{\mathrm{eff}}^{\mathrm{T}}, \tag{11}$$

in which D_i^{M} is a mixture-averaged diffusion coefficient for species i, and $D_{\mathrm{eff}}^{\mathrm{T}}$ is an effective coefficient accounting for turbulent mixing [44]. The expression for D_i^{M} is calculated according to [45] as

$$D_i^{\mathrm{M}} = \frac{1 - y_i}{\sum_{j\neq i}\frac{x_j}{\mathcal{D}_{i,j}}}, \tag{12}$$

where $\mathcal{D}_{i,j}$ is the binary diffusion coefficient for the (i, j) pair of species, derived from first order collision integrals [46]. In particular, collision integrals for neutral–neutral and electron–neutral interactions are taken from the work by Laricchiuta *et al* [47], while electron–electron and electron–ion collision integrals are tabulated by Mason *et al* [48]. In case of an electron–heavy species interaction, the collision integrals are computed at the reduced temperature given by $T^* = (m_{\mathrm{e}}T_{\mathrm{g}} + m_i T_{\mathrm{e}})/(m_{\mathrm{e}} + m_i)$, with m_{e} and m_i the electron and heavy species mass, respectively, T_{e} and T_{g} the electron and the gas temperature, respectively [49]. Note that equation (12), also used by Kubečka *et al* [50] and by Baeva *et al* [42], is a generalized Fick expression that is strictly valid under the trace-species approximation [51]. A self-consistent approach to describe mass diffusion in a multi-component mixture is based on the solution of momentum balance equations, as defined in [52, 53]. This approach has been considered in [24], where the Stefan–Maxwell equations have been solved numerically together with mass balance equations for a CO_2–CO–O_2–O–C mixture. Nevertheless, we note that, for the conditions under consideration in this work, deviations between neutral species mole fractions obtained using equation (12) and the ones obtained by a self-consistent model based on the solution of the Stefan–Maxwell equations do not exceed a few percent. The expression for the effective turbulent diffusion coefficient $D_{\mathrm{eff}}^{\mathrm{T}}$ is taken from [30, 54] as

$$D_{\mathrm{eff}}^{\mathrm{T}} = \frac{\nu_{\mathrm{T}}}{Sc_{\mathrm{T}}}, \tag{13}$$

where ν_{T} is the turbulent kinematic viscosity, and $\mathrm{Sc_T}$ is the turbulent Schmidt number. In particular, supported by computational fluid dynamics simulations of the vortex flow including a heat source representing the plasma [30], it is assumed that ν_{T} has a quadratic profile as a function of the radius:

$$\nu_{\mathrm{T}}(r) = \nu_{\mathrm{T}}(0)\left[1 - \left(\frac{r}{R_{\mathrm{in}}}\right)^2\right], \tag{14}$$

where R_{in} is the tube inner radius, and the value of the coefficient $\nu_{\mathrm{T}}(0)$ is taken from the work by Wolf *et al* [30]. Note that $\nu_{\mathrm{T}}(0)$ exhibits a dependence on both gas pressure and gas flow rate, as described in [30]. A value of $\mathrm{Sc_T} = 0.7$ is considered in equation (13), as in works considering comparable gas flow rates [55].

The ambipolar diffusion theory, as reported by Oskam [56], for multi-ionic plasmas is used to describe the charged species radial transport. The same approach has been adopted by Hassouni *et al* [41] and by Wang *et al* [28]. According to Oskam's theory, the ambipolar field is

$$E_{\mathrm{amb}} = \left(\sum_i \mu_i n_i\right)^{-1}\left(\sum_i \frac{q_i}{|q_i|} D_i \frac{\mathrm{d}n_i}{\mathrm{d}r}\right), \tag{15}$$

where the summation runs over all charged species including electrons, and the mobilities of different charged species μ_i are calculated using the Einstein relation, from the gas temperature T_{g} and the corresponding mixture-averaged diffusion coefficient at every radial position [54]. Note that Oskam's model has been derived assuming that the total current density and the total charge density obtained by summing over all species are both equal to zero [56]. These assumptions are typically violated when the plasma contains several ion species [42]. However, as it will be shown in subsection 4.2, O_2^+ ion is the dominant ion for a diffuse plasma, over the whole radius, and for a contracted plasma, further than 1 mm from the center of the tube. Hence, we expect that the current ambipolar diffusion model is still accurate, for the conditions under considerations.

The electron mass fraction is calculated from quasi-neutrality as

$$y_{\mathrm{e}} = \frac{m_{\mathrm{e}}}{q_{\mathrm{e}}} \sum_{i \neq \mathrm{e}} \frac{q_i}{m_i} y_i, \tag{16}$$

where the summation runs over all charged species, except electrons [40]. Note that, due to the usage of effective diffusion coefficients in equation (11), it is not guaranteed that diffusive mass fluxes sum up to zero. In other words, the continuity equation for the mixture as a whole does not hold. Hence, the mass fraction of CO_2 is obtained by enforcing the mass conservation as

$$y_{\mathrm{CO_2}} = 1 - \sum_{i \neq \mathrm{CO_2}} y_i, \tag{17}$$

where the summation runs over all charged and neutral species, except CO_2. Furthermore, the species mole fractions are derived from the respective mass fractions according to the relation

$$x_i = y_i \frac{m}{m_i}. \tag{18}$$

In section 4, the species molar fractions calculated from the model are compared with the ones derived from experimental measurements.

3.2. Gas temperature equation

In the model, neutrals and ions are characterized by a translational temperature T_{g}. Moreover, supported by detailed experimental observations [10, 12], it is assumed that, at steady-state, the translational, rotational and vibrational temperatures of the molecules have all the same value T_{g}, that is calculated from the following energy equation:

$$-\frac{1}{r}\frac{\mathrm{d}}{\mathrm{d}r}\left(r\lambda\frac{\mathrm{d}T_{\mathrm{g}}}{\mathrm{d}r}\right) + \sum_i \frac{1}{r}\frac{\mathrm{d}}{\mathrm{d}r}\left(rJ_i h_i\right) = P_{\mathrm{in}}(r) - Q_{\mathrm{flow}} - Q_{\mathrm{rad}}, \tag{19}$$

where λ is the heat conductivity of the mixture, J_i is the mass diffusive flux of species i (equation (10)), h_i is the enthalpy of species i, $P_{\mathrm{in}}(r)$ is the MW power density that is locally absorbed by the electrons, Q_{flow} is the heat loss due to convection by the axial flow, and Q_{rad} is the energy lost from the plasma by radiation.

The heat conductivity in equation (19) is calculated as the sum of a mixture-averaged conductivity $\lambda_{\mathrm{g}}^{\mathrm{M}}$ and an effective turbulent conductivity $\lambda_{\mathrm{eff}}^{\mathrm{T}}$, as proposed by Gleizes *et al* [44]:

$$\lambda = \lambda_{\mathrm{g}}^{\mathrm{M}} + \lambda_{\mathrm{eff}}^{\mathrm{T}}. \tag{20}$$

A semi-empirical formula is used for calculations of $\lambda_{\mathrm{g}}^{\mathrm{M}}$:

$$\lambda_{\mathrm{g}}^{\mathrm{M}} = \frac{1}{2}\left[\sum_i x_i\lambda_i + \left(\sum_i \frac{x_i}{\lambda_i}\right)^{-1}\right], \tag{21}$$

which is only dependent on the species molar fractions x_i, and on the pure species heat conductivities λ_i. According to Mathur *et al* [57], this expression gives results with errors in the range of a few percent. Moreover, in 1D model calculations, equation (21) is preferred to other semi-empirical formulas, such as the one proposed by Wilke [58], since it does not require computations of single species gas viscosities. The pure species quantities λ_i are cast in a polynomial form, where the coefficients of the polynomials are tabulated in the NASA library [59]. The effective turbulent component of the heat conductivity is written as

$$\lambda_{\mathrm{eff}}^{\mathrm{T}} = \rho C_{p,\mathrm{mix}} \frac{\nu_{\mathrm{T}}}{\mathrm{Pr_T}}, \tag{22}$$

where $\mathrm{Pr_T}$ is the turbulent Prandtl number, and $C_{p,\mathrm{mix}}$ is the mixture-averaged specific heat. A value of 0.85 is used for $\mathrm{Pr_T}$, as in simulations for a similar setup [30]. Moreover, the expression of $C_{p,\mathrm{mix}}$ is defined as

$$C_{p,\mathrm{mix}} = \sum_i C_{p,i} y_i, \tag{23}$$

where $C_{p,i}$ is the specific heat of species i [51]. The pure species quantities, h_i and $C_{p,i}$, in equations (19) and (23) are taken from a NASA technical report [60].

The loss of heat due to convective cooling by the axial gas flow is accounted for in equation (19), by a term depending on the axial flow speed (equation (8)) and on the plasma length

$$Q_{\text{flow}} = \left[\rho C_{p,\text{mix}} T_\text{g} - \left(\rho C_{p,\text{mix}} T_\text{g}\right)_\text{env}\right] \frac{v_\text{axial}}{L}, \tag{24}$$

where the subscript 'env' denotes the environment species composition and temperature, that is considered as pure CO_2 at 300 K. A similar expression has been taken into account by Wang *et al* [28]. The radiation transfer term in equation (19) is calculated as

$$Q_\text{rad} = 4\pi\epsilon_\text{N}, \tag{25}$$

where ϵ_N is the net emission coefficient of radiation, for a given temperature. The values of ϵ_N are taken from the work by Aubrecht and Bartlova [61], where ϵ_N is computed for a thermal CO_2 plasma, at various pressures and plasma thickness.

The local absorbed MW power density in equation (19) is estimated from measurements of the total plasma emissivity as

$$P_\text{in}(r) = P_\text{in}(0) \exp\left[-\frac{1}{2}\left(\frac{r}{W/2}\right)^2\right]. \tag{26}$$

The same expression for $P_\text{in}(r)$ has been adopted by Wolf *et al* [30] and the validity of equation (26) has been discussed in details by Viegas *et al* [38]. We note that results of the model are highly dependent on the choice of the input peak MW power density ($P_\text{in}(0)$). Hence, accurate estimations or measurements of $P_\text{in}(0)$ are sought after. In subsection 4.4, the effect of the uncertainties on experimental estimation is $P_\text{in}(0)$ on the model results are presented. The power density loss is also calculated from MCF as

$$\text{P}_\text{calc}(r) \approx n_\text{e}\left(Q_\text{e,el} + Q_\text{e,inel}\right), \tag{27}$$

where the expressions for the elastic ($Q_\text{e,el}$) and inelastic ($Q_\text{e,inel}$) electron power losses are taken from [62] as

$$Q_\text{e,el} = \sum_i \frac{2m_\text{e}}{m_i}\langle\nu_{ei}\epsilon\rangle, \tag{28}$$

$$Q_\text{e,inel} = \sum_j V_j\left(\langle\nu_{ej}\rangle - \langle\nu_{ej}^\text{inv}\rangle\right), \tag{29}$$

where ν_{ei} is the microscopic collision frequency for an electron of energy ϵ which results in a transfer of momentum to the ith species, ν_{ej} is the microscopic collision frequency for inelastic collisions of electrons with the jth species, V_j is the corresponding energy threshold, ν_{ej}^inv is the microscopic collision frequency of the superelastic inverse process of each individual excitation process, and the symbol $\langle\cdot\rangle$ represents the average of the quantity within the brackets over the EEDF. Additionally, in the model, the electron temperature is defined as $k_\text{B}T_\text{e} = 2\langle\epsilon\rangle/3$, where $\langle\epsilon\rangle$ is the electron mean energy, although the EEDF deviates from a Maxwell–Boltzmann distribution. The local value of E/n is determined through an iterative procedure until the condition $P_\text{in}(r) \approx P_\text{calc}(r)$ is met, as described in subsection 3.4. Note that equation (27) is an approximate form of the electron energy balance equation that is valid when electrons are close to local field equilibrium and the electron energy transport terms are negligible [63]. This assumption is valid for the conditions under consideration as the energy exchanges through inelastic collisions of electrons are the dominant contribution in the electron energy equation [23].

According to Dalton's law, the static pressure p_g is defined as the sum of the partial pressures of the different species, thus leading to

$$p_\text{g} = \sum_{i\neq\text{e}} n_i k_\text{B} T_\text{g} + n_\text{e} k_\text{B} T_\text{e}. \tag{30}$$

Equation (30) is used as local constraint to determine the total gas number density.

3.3. Boundary conditions

In the center of the tube, due to axial symmetry, a homogeneous Neumann boundary condition for the neutral species mass fractions and gas temperature has been considered.

A flux boundary condition has been used for neutrals and ions at the tube wall (i.e. at $r = R_\text{in}$) [64, 65]:

$$\boldsymbol{J}_i \cdot \boldsymbol{n} = \rho\gamma_i \left[H(\text{sgn}(q_i)\mu_i E_\text{amb})\frac{q_i}{|q_i|} y_i \mu_i \boldsymbol{E}_\text{amb} \cdot \boldsymbol{n} + \frac{1}{4} y_i v_{\text{th},i} - \frac{1}{2} D_i \nabla y_i \cdot \boldsymbol{n}\right], \tag{31}$$

where $\boldsymbol{n}$ is the normal vector pointing towards the wall, $H(\text{sgn}(q_i)\mu_i E_\text{amb})$ is the Heaviside step-function that is set to one if the drift velocity is directed towards the wall and to zero otherwise, $v_{\text{th},i}$ is the thermal velocity of the ith species, i.e.

$$v_{\text{th},i} = \sqrt{\frac{8k_\text{B}T_\text{g}}{\pi m_i}}, \tag{32}$$

and γ_i is the fraction of particles that is adsorbed at the surface that is set to 10^{-3} for neutral species, based on similar values for adsorption of O atoms in silica-like walls [66], and it is assumed to be equal to 1 for the ions [41]. Moreover, recombination of atomic species into molecular ones the surface and secondary electron emission from the surface are not taken into account in the model. Note that the aforementioned assumptions on adsorption probabilities do not have an important influence on the model results for the conditions under consideration [67]. In fact, the species concentration in the MW reactor is mainly determined by the gas phase chemistry and not by surface reactions.

At the quartz wall boundary, the heat flux (J_g) is assumed to be continuous [40], such that

$$J_\text{g}|_\text{wall} = -\frac{\lambda_w\left(T_\text{g,env} - T_\text{g}(R_\text{in})\right)}{R_\text{in}\,\log\frac{R_\text{out}}{R_\text{in}}}, \tag{33}$$

where $R_\text{in} = 13.5$ mm is the inner tube radius of the reactor, the thickness of the quartz tube is 1.5 mm, such that the outer radius is $R_\text{out} = 15$ mm, λ_w is the quartz tube heat conductivity, that is assumed to have a constant value of 1.4 W m^{-1} K^{-1}, and $T_\text{g,env}$ is the environment temperature for the outside part of the wall and it is set to 300 K.

3.4. Numerical solutions of the fluid equations and coupling with Monte Carlo flux

The finite volume method has been used to discretize the fluid equations (5) and (19) [68, 69]. As such, all the variables and sources have been defined at cell centers (i.e. the nodal points of the grid), whereas fluxes are defined at cell interfaces. The exponential scheme by Scharfetter and Gummel [70] has been employed for the discretization coefficients. The tridiagonal matrix algorithm has been employed for matrix inversion.

The fluid model is coupled to an MCF code, that provides calculations of the EEDFs, T_e, electron rate and transport coefficients and electron power losses (equations (28) and (29)) in each cell node, for a given E/n profile and composition. The composition and E/n are calculated through an iterative procedure. The principles of the iterative solution procedure are similar to the ones adopted by Hassouni *et al* [67] and the schematic of the fluid-MCF model implementation is shown in figure 3. The simulation starts by setting different input parameters, such as the profile of MW deposited power ($\mathrm{MWPD_{inp}}(r)$), the pressure of the gas (p_g) and the gas flow rate (Φ), and an initial guess for profiles of reduced electric field (E/n), species mass fractions (y_i), gas temperature (T_g), and reduced angular frequency of the field (ω/n). A first set of MCF simulations is performed, in order to obtain estimations of the electron parameters averaged over the EEDF, under the aforementioned initial condition. In order to reduce the CPU time associated to MCF simulations, MCF runs are performed only for nodal points labelled by odd-indexes in the grid. Hence, a linear interpolation of MCF outputs from the odd-index to the even-index nodal points is performed. The accuracy of the calculations is expected to be affected no more than a few percent by this procedure, due to the high number of cells that are used in the grid leading to a cell size lower than 0.1 mm. The fluid model calculation starts by computing transport properties, thermodynamic parameters and source terms that are used for the numerical solution of the mass and energy balance equations (equations (5) and (19)). A first check is performed to ensure that the species composition and gas temperature reach numerical steady state. The numerical steady state is reached when the residuals of y_i and T_g are lower than a pre-defined tolerance (ϵ), that is set to 10^{-6}. Typically, around 10 000 iterations are required for this condition to be fulfilled. Once the steady-state is reached, the MW power losses are computed from equation (27). The discharge maintaining E/n is determined by the condition that $|P_{\mathrm{calc}}(r) - P_{\mathrm{in}}(r)| < \epsilon'$, where ϵ' is the tolerance for the power balance between the MW power deposited and the power losses by the plasma, that is set to 10^{-2}. In this case, the E/n profile is adjusted iteratively in the code by multiplying the E/n found from the previous iteration by a term proportional to $(P_{\mathrm{calc}}(r) - P_{\mathrm{in}}(r))$, in order to fulfil the aforementioned condition. Typically, around ten iterations are required to satisfy the power balance relation. Note that, if E/n is updated, also MCF simulations are repeated, taking into account the updated composition calculated from the fluid model.

All the calculations presented in section 4 have been performed with a uniform grid of 150 cells, from the center of the tube to the inner tube radius. The total number of cells has been chosen in order to guarantee uniformity in the calculated quantities and source terms within the control volumes, as required by the finite volume approach [69]. A relaxation factor of 0.99 is applied on discretization coefficients and chemical source terms of mass balance equations [71]. As initial condition, the electron and O_2^+ ion number densities are set to be equal to 10^2 cm^{-3} in the whole domain. Moreover, a background CO_2 gas at 300 K is considered as initial condition of the simulation. The total CPU time for a fluid-MCF simulation is up to 15 h on a 2.6 GHz Intel i7 single core processor, mostly due to the iterations required for the MW power deposited to be equal to the power lost.

3.5. Reaction scheme

The reactions scheme used in this work is mostly taken from the work by Viegas *et al* [23], that is an improvement of previous works by Kozák and Bogaerts [18] and by Koelman *et al* [19] for application to CO_2 MW plasmas at intermediate pressures. In this subsection, the main features of that scheme are summarized, together with the changes in the chemistry set that have been adopted for this work.

3.5.1. Thermal chemistry. The reactions scheme for neutral-neutral collisions has been taken from the GRI-MECH 3.0 database [72]. In particular, table 3 presents forward reaction rate coefficients ($k_{f,i}$) for CO_2, CO, O_2, O and C. Moreover, in van de Steeg *et al* [10] it has been shown that the use of this dataset of reactions gives the best agreement between calculations and experiments of total (volume averaged) CO production and input MW power, where $k_{0,i}$ is the low-pressure limit rate coefficient, whose expression is taken from [72]. The rate coefficients for the reverse reactions ($k_{r,i}$) have been obtained considering that, at equilibrium, the rate-of-progress of all reactions is zero, which yields the following relationship between the forward and backward rate coefficients

$$\frac{k_{f,i}}{k_{r,i}} \equiv K_{eq,i}, \tag{34}$$

where $K_{eq,i}$ is the equilibrium constant for the ith reaction [73]. The equilibrium constant is related to the change in Gibbs free energy across a reaction ΔG_i by

$$K_{eq,i} = \left(\frac{p_g}{RT_g}\right)^{\Delta\nu_i} \exp\left(-\frac{\Delta G_i}{RT_g}\right), \tag{35}$$

where $\Delta\nu_i$ is the difference between the stoichiometric coefficients of products and reactants. Additionally, according to [23], it is assumed that, at steady state and for the high T_g calculated in the plasma core, electronically excited species have a negligible contribution, and all vibrational/rotational states of the ground electronic state of the molecules are in thermal equilibrium, as measured by van de Steeg *et al* [10].

3.5.2. Electron impact reactions. Electron impact reactions used in the fluid model can be found in table 4, where all neutral and charged collision partner species have been considered

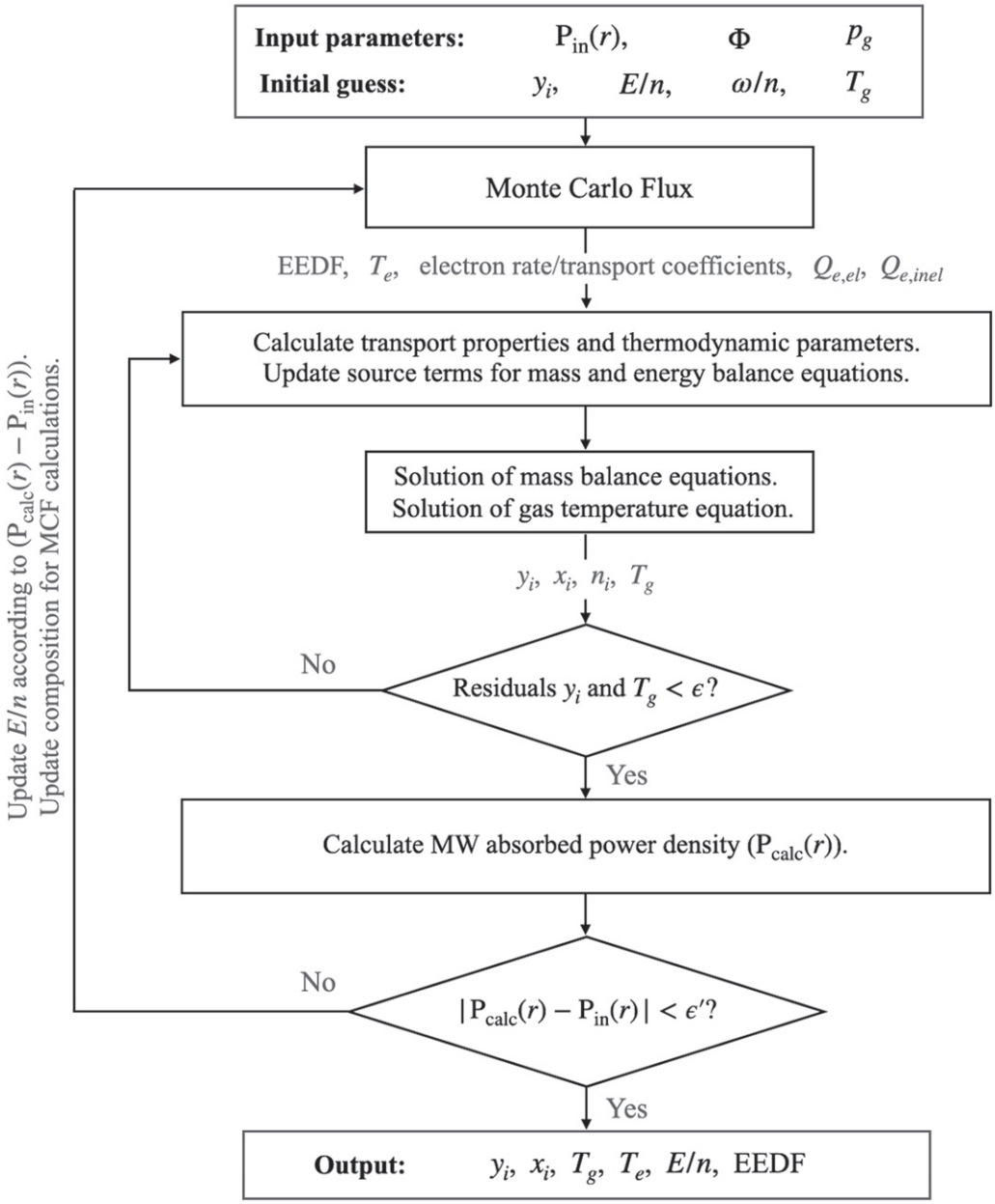

Figure 3. Workflow of the fluid-MCF model. See text for a detailed description of the iterative procedure. Note that MCF is run locally for each point along the radial coordinate.

in their ground electronic state. For a collision of an electron with a neutral atom/molecule, the reaction rate coefficient is given by

$$k_j = \sqrt{\frac{2q_e}{m_e}} \int_0^\infty \sigma_j(\epsilon) f_0(\epsilon) \epsilon \, \mathrm{d}\epsilon, \tag{36}$$

where ϵ is the electron kinetic energy, k_j and $\sigma_j(\epsilon)$ are the electron impact rate coefficient for the jth collisional process and the corresponding cross section, respectively, and $f_0(\epsilon)$ is the EEDF that is calculated from MCF. Normalization of the EEDF is such that

$$\int_0^\infty f_0(\epsilon) \sqrt{\epsilon} \, \mathrm{d}\epsilon = 1. \tag{37}$$

Due to a lack of cross sections for electron–ion interactions (E20–25), rate coefficients for those reactions have been computed from expressions that are uniquely dependent on the electron temperature (T_e).

In addition to the reactions reported in table 4, the following processes have been included for accurate EEDFs calculations in MCF. Note that those processes are not included in the fluid model reactions scheme, but only in MCF. In particular, electron impact cross sections with CO_2 molecules have been taken from the Biagi database of LXCat [74]. Specifically, the elastic momentum transfer for the ground electronic state of CO_2 has been modified by taking into account a Boltzmann population at T_g of the excited vibrational levels of the ground electronic state and rotational levels of the ground vibrational state, as described in [37]. Additionally, cross sections for

Table 3. List of neutral thermal chemistry reactions. Rate coefficients are provided for the forward reactions. Rate coefficients for the reverse reactions are calculated assuming thermodynamic equilibrium. Units for rate coefficients for two-body reactions are $cm^3\ s^{-1}$ and for three-body reactions are $cm^6\ s^{-1}$, n is the total number density in cm^{-3}, P_r is the reduced pressure as defined in [72], and T_g is the gas temperature in K.

#	Reaction	Forward rate coefficient	Ref.
N1	$O + O + CO \leftrightarrow O_2 + CO$	$5.79 \times 10^{-31} T_g^{-1}$	[72]
N2	$O + O + CO_2 \leftrightarrow O_2 + CO_2$	$11.92 \times 10^{-31} T_g^{-1}$	[72]
N3	$O + CO + CO \leftrightarrow CO_2 + CO$	$4.49 \times 10^{-14} \exp(-1195.27/T_g) \cdot \frac{P_r}{n(1+P_r)}$	[72]
N4	$O + CO + CO_2 \leftrightarrow CO_2 + CO_2$	$10.47 \times 10^{-14} \exp(-1195.27/T_g) \cdot \frac{P_r}{n(1+P_r)}$	[72]
N5	$O + CO + O_2 \leftrightarrow CO_2 + O_2$	$17.94 \times 10^{-14} \exp(-1195.27/T_g) \cdot \frac{P_r}{n(1+P_r)}$	[72]
N6	$O_2 + CO \leftrightarrow CO_2 + O$	$4.15 \times 10^{-12} \exp(-24\,021.37/T_g)$	[72]
N7	$CO + CO \leftrightarrow CO_2 + C$	$6.31 \times 10^{-11} \exp(-97\,013.83/T_g)$	[72]
N8	$CO + O \leftrightarrow C + O + O$	$3.57 \times 10^{3} T_g^{-3.1} \exp(-1288.10/T_g)$	[72]
N9	$CO + O_2 \leftrightarrow C + O + O_2$	$3.57 \times 10^{3} T_g^{-3.1} \exp(-1288.10/T_g)$	[72]
N10	$CO + CO \leftrightarrow C + O + CO$	$14.28 \times 10^{3} T_g^{-3.1} \exp(-1288.10/T_g)$	[72]
N11	$CO + CO_2 \leftrightarrow C + O + CO_2$	$7.14 \times 10^{3} T_g^{-3.1} \exp(-1288.10/T_g)$	[72]
N12	$O_2 + C \leftrightarrow CO + O$	$5.36 \times 10^{-12} T_g^{0.41} \exp(26.92/T_g)$	[72]

electron impact dissociation of CO_2 have been taken from the work by Polak and Slovetsky [81], as the calculated rate coefficients from these cross sections are comparable with experimental measurements [37, 84]. According to the recommendation by Morillo-Candas *et al* [84], Polak and Slovetsky's cross sections have not been included in MCF simulations, but they have been used only for the calculations of the corresponding rate coefficients. The use of Polak and Slovetsky's cross sections within the Biagi's set of electron impact cross sections has been found to provide good agreement between calculated and measured total dissociation rate coefficients, within a few percent, for E/n up to 110 Td [37]. The total ionization cross section from the Biagi database has been replaced by the ones taken from the Itikawa database of LXCat [75] that reproduce the same total ionisation cross section, but include also the dissociative contribution to the formation of different ions. Fridman's approximation [9] has been used to obtain electron impact cross sections for stepwise excitations from excited vibrational levels, from $\nu = 1$ to $\nu = 21$ for the asymmetric stretching vibrational mode of the ground electronic state. The same approximation has been adopted by Pietanza *et al* [22] and by Berthelot and Bogaerts [85]. Superelastic collisions cross sections from vibrationally excited states of the ground electronic state of CO_2 have been calculated using the formula of Klein–Rosseland [86].

Electron impact cross sections with CO molecules have been taken from Biagi's code Magboltz v11.10 [76]. This set replaces the IST-Lisbon dataset [87] that has been used in the work by Viegas *et al* [23]. Anisotropic scattering for rotational collisions has been included according to the dipole-Born anisotropic scattering model described in [88]. As for the CO_2 cross sections set, the total ionization cross section from Magboltz v11.10 has been replaced with different dissociative ionization cross sections that are included in the Itikawa database of LXCat [75]. Cross sections from the work by Laporta *et al* [89] for electron impact vibrational excitations from vibrational levels of the ground electronic state have been included, for levels from $\nu = 1$ to $\nu = 80$. These cross sections have not been included in our previous work [23], but they are present in the work by Pietanza *et al* [22]. The population of rotational and vibrational levels has been considered as a Boltzmann distribution at T_g. Moreover, superelastic collisions from those levels have been included using the micro-reversibility principle [86]. Additionally, note that electron impact dissociation of CO molecules in the ground electronic state is not included in the Biagi's set. Therefore, the cross section for this process has been taken from the work by Cosby [90]. The same cross section has been included in the recent IST-Lisbon set [87].

As in [23], electron impact cross sections with O atoms and C atoms are taken from the IST-Lisbon [77] and the B-spline atomic R-matrix databases [78], respectively.

Electron impact cross sections with O_2 molecules are taken from the Biagi database of LXCat [74]. These cross sections replace the ones from the IST-Lisbon database [77] considered in [23]. Indeed, Biagi's cross sections have been preferred to the IST-Lisbon ones due to (i) consistency with the MCF method used in this work, and (ii) the use of an elastic momentum transfer cross section, instead of the effective cross section that is proposed in [77]. Ionization cross sections have been taken from the Itikawa dataset [75], in replacement of the total ionization cross section that is included in the Biagi's set. A Boltzmann distribution for the first 11 vibrational levels (i.e. $\nu = 0$–10) of the ground electronic state of O_2 has been considered. Moreover, stepwise vibrational excitations/de-excitations between vibrational states characterized by quantum numbers from $\nu = 0$ to $\nu = 10$ have been included. Cross sections for these processes have been taken from the work by Laporta *et al* [91]. Electron impact de-excitation cross sections have been calculated using the Klein–Rosseland formula [86].

In this work it is also assumed that the plasma is weakly ionized, such that self-collisions of electrons (i.e. electron–electron collisions) are negligible. This assumption is discussed in more detail in section 4.

3.5.3. Ion–ion and ion–neutral reactions. Ionic conversion (I1–20), electron detachment (I21–24), ion–ion collisions

Table 4. List of charged particle reactions: electron-impact ionisation, attachment and dissociation; electron–ion recombination. Units for rate coefficients for two-body reactions are $cm^3\ s^{-1}$ and for three-body reactions are $cm^6\ s^{-1}$, T_e is the electron temperature, in K, for reaction E5 and in eV for the remaining reactions, M represents any neutral species, and T_g is the gas temperature in K. For other rate coefficients labelled by EEDF, the value is calculated from the EEDFs computed with the MCF. Note that these reactions are used in the fluid model. See text for a description of electron impact reactions included only in the MCF solver.

#	Reaction	Rate coefficient	Ref.
E1	$e + CO_2 \rightarrow CO_2^+ + 2e$	EEDF	[74, 75]
E2	$e + CO_2 \rightarrow CO + O^+ + 2e$	EEDF	[74, 75]
E3	$e + CO_2 \rightarrow O + CO^+ + 2e$	EEDF	[74, 75]
E4	$e + CO_2 \rightarrow O_2 + C^+ + 2e$	EEDF	[74, 75]
E5	$e + CO_2 \rightarrow C + O_2^+ + 2e$	$7 \times 10^{-13} T_e^{0.5}(1 + 1.3 \times 10^{-5} T_e)\exp(\frac{-1.5\times10^5}{T_e})$	[17]
E6	$e + CO \rightarrow CO^+ + 2e$	EEDF	[75, 76]
E7	$e + CO \rightarrow O + C^+ + 2e$	EEDF	[75, 76]
E8	$e + CO \rightarrow C + O^+ + 2e$	EEDF	[76, 77]
E9	$e + O_2 \rightarrow O_2^+ + 2e$	EEDF	[74, 75]
E10	$e + O_2 \rightarrow O + O^+ + 2e$	EEDF	[74, 75]
E11	$e + O \rightarrow O^+ + 2e$	EEDF	[77]
E12	$e + C \rightarrow C^+ + 2e$	EEDF	[78]
E13	$e + CO_2 \rightarrow CO + O^-$	EEDF	[74]
E14	$e + CO \rightarrow C + O^-$	EEDF	[76]
E15	$e + O_2 \rightarrow O + O^-$	EEDF	[74]
E16	$e + O + M \rightarrow O^- + M$	10^{-31}	[79, 80]
E17	$e + CO_2 \rightarrow e + CO + O$	EEDF	[74, 81]
E18	$e + CO \rightarrow e + C + O$	EEDF	[76, 77]
E19	$e + O_2 \rightarrow e + O + O$	EEDF	[74]
E20	$e + CO_2^+ \rightarrow CO + O$	$3.94 \times 10^{-7} T_e^{-0.4}$	[17]
E21	$e + CO_2^+ \rightarrow C + O_2$	$3.94 \times 10^{-7} T_e^{-0.4}$	[17]
E22	$e + CO^+ \rightarrow C + O$	$1.57 \times 10^{-7} T_e^{-0.4}$	[17]
E23	$e + O_2^+ + M \rightarrow O + O + M$	$1.61 \times 10^{-27} T_e^{-0.5}$	[17]
E24	$e + O_2^+ \rightarrow O + O$	$5.17 \times 10^{-9} T_e^{-1} + 1.51 \times 10^{-8} T_e^{-0.7}$	[82]
E25	$e + O^+ + M \rightarrow O + M$	$2.49 \times 10^{-29} T_e^{-1.5}$	[83]

(I25–28) are reported in table 5. Most of the rate coefficients for these reactions have been taken from the work by Beuthe and Chang [17] and by Viegas *et al* [23].

3.5.4. Associative ionization. Associative ionization reaction rate coefficients are reported in table 6 (reactions A1–3). In particular, as described in section 4.2, associative ionization reactions are particularly important at high pressures (i.e. above 100 mbar), since they are the main sources of electron production. The expression for the rate coefficients has been taken from the work by Park *et al* [94] as

$$k_{ai} = C\left(\frac{T_g[\mathrm{K}]}{6000}\right)^{\alpha} \exp\left(-\frac{E_a}{T_g[\mathrm{K}]}\right), \tag{38}$$

where the values for the coefficients C and α and for the activation energy E_a (in K) are given in [96], and T_g[K] is the gas temperature in K. Note that these rate coefficients have positive pre-exponential powers (i.e. $\alpha \geqslant 1$). However, as stated by Park [96], it is unlikely that α would remain positive for T_g above 6000 K. Therefore, in this work, $\alpha = 0$ has been assumed. The resulting expression for k_{ai} is then equivalent to an extrapolation of these reaction rate coefficients for gas temperatures above 6000 K, as recommended by Park [96].

4. Results

4.1. Neutral species composition and gas temperature

In this subsection, calculated neutral species mole fractions and gas temperature along the tube radius, corresponding to the center of the discharge vessel in the axial direction, are shown. Results of the calculations have been compared with measurements obtained by means of Raman scattering [13, 24]. The input parameters for the model are given in table 1.

The measured and calculated gas temperatures for the 100 mbar and 150 mbar cases are shown in figures 4(a) and (b), respectively. These conditions have been chosen as examples of a diffuse and a contracted discharge. Specifically, the calculated T_g is up to 4900 K and 7200 K for the 100 mbar and 150 mbar cases, respectively. As a result of the higher peak in the MW power density ($P_{in}(0)$), the contracted case is characterized by (i) higher gas temperature in the center of the tube, and (ii) larger gradients in the radial profiles (figure 4(b)), than in the diffuse case. As shown in subsection 4.2, the non-uniformity of T_g affects also the spatial distribution of charged species concentrations. Overall, a good agreement has been found between measurements and calculations of T_g, within

Table 5. List of charged particle reactions: ion transfers, detachment, ion–ion recombination. Units for rate coefficients for two-body reactions are $cm^3\ s^{-1}$ and for three-body reactions are $cm^6\ s^{-1}$. M represents any neutral species and T_g is the gas temperature in K.

#	Reaction	Rate coefficient	Ref.
I1	$CO_2 + O^+ \rightarrow CO + O_2^+$	4.5×10^{-10}	[17]
I2	$CO_2 + O^+ \rightarrow O + CO_2^+$	4.5×10^{-10}	[17]
I3	$CO_2 + C^+ \rightarrow CO + CO^+$	1.1×10^{-9}	[17, 92]
I4	$CO_2 + CO^+ \rightarrow CO + CO_2^+$	1.0×10^{-9}	[17, 79, 80, 92]
I5	$CO + O^+ \rightarrow O + CO^+$	$2.83 \times 10^{-13} T_g^{0.5} \exp(-4580/T_g)$	[92]
I6	$CO + C^+ \rightarrow C + CO^+$	5.0×10^{-13}	[17, 92]
I7	$C + CO^+ \rightarrow CO + C^+$	1.1×10^{-10}	[93]
I8	$C + O_2^+ \rightarrow O + CO^+$	5.2×10^{-11}	[93]
I9	$C + O_2^+ \rightarrow O_2 + C^+$	5.2×10^{-11}	[93]
I10	$O + CO_2^+ \rightarrow CO + O_2^+$	1.64×10^{-10}	[93]
I11	$O + CO_2^+ \rightarrow CO_2 + O^+$	9.62×10^{-11}	[93]
I12	$O_2 + CO_2^+ \rightarrow CO_2 + O_2^+$	6.4×10^{-11}	[17]
I13	$O + CO^+ \rightarrow CO + O^+$	1.4×10^{-10}	[17, 93, 94]
I14	$O_2 + CO^+ \rightarrow CO + O_2^+$	1.2×10^{-10}	[17, 92, 93]
I15	$O_2 + C^+ \rightarrow CO + O^+$	6.14×10^{-10}	[17]
I16	$O_2 + C^+ \rightarrow O + CO^+$	3.8×10^{-10}	[17, 92]
I17	$O_2 + O^+ \rightarrow O + O_2^+$	$3.29 \times 10^{-10} T_g^{-0.5}$	[17, 92]
I18	$O + O^+ + M \rightarrow O_2^+ + M$	1.0×10^{-29}	[83]
I19	$O + O_2^+ \rightarrow O_2 + O^+$	$6.64 \times 10^{-12} T_g^{-0.09} \exp(-18\,000/T_g)$	[94]
I20	$O_2 + C^+ \rightarrow C + O_2^+$	$1.66 \times 10^{-11} \exp(-9400/T_g)$	[94]
I21	$CO + O^- \rightarrow CO_2 + e$	5.5×10^{-10}	[17, 92]
I22	$O + O^- \rightarrow O_2 + e$	1.9×10^{-9}	[17]
I23	$M + O^- \rightarrow M + O + e$	6.9×10^{-10}	[17]
I24	$C + O^- \rightarrow CO + e$	5.0×10^{-10}	[93]
I25	$O^+ + O^- \rightarrow O + O$	$4.65 \times 10^{-7} T_g^{-0.43}$	[95]
I26	$O^+ + O^- + M \rightarrow O_2 + M$	$1.56 \times 10^{-19} T_g^{-2.5}$	[17]
I27	$O_2^+ + O^- \rightarrow O_2 + O$	$3.20 \times 10^{-7} T_g^{-0.44}$	[95]
I28	$O_2^+ + O^- \rightarrow O + O + O$	$5.17 \times 10^{-6} T_g^{-0.44}$	[95]

Table 6. List of associative ionization reactions. T_g is the gas temperature in K.

#	Reaction	Rate coefficient ($cm^3\ s^{-1}$)	Ref.
A1	$O + O \rightarrow O_2^+ + e$	$1.86 \times 10^{-11} \exp(-80\,600/T_g)$	[94]
A2	$C + O \rightarrow CO^+ + e$	$8.78 \times 10^{-12} \exp(-33\,100/T_g)$	[94]
A3	$CO + O \rightarrow CO_2^+ + e$	$1.86 \times 10^{-11} \exp(-80\,600/T_g)$	[94]

the first 10 mm. In this respect, note that the expression for turbulent viscosity that has been used in this work (equation (14)) is taken from the work by Wolf *et al* [30], in order to ensure that radial turbulent transport is representative of the experimental conditions.

Measured and calculated mole fractions for the main neutral species (CO_2, CO, O, O_2, and C) for the 100 mbar and 150 mbar cases are shown in figures 5(a) and (b), respectively. The agreement is good. In particular, figure 5 shows that the transition from a diffuse (100 mbar) to a contracted (150 mbar) discharge is accompanied by a change in neutral species composition, from a partially dissociated to a fully dissociated core, near the center of the tube. This transition is a direct consequence of the increase in the peak T_g showed in figure 4. The highest discrepancies between simulation results and experiments have been found for the O atom mole fractions at 150 mbar (figure 5(b)), for radial positions within 5 mm. These discrepancies can be due to (i) an underestimation of the O atom formation rates from thermal dissociation of CO and O_2 at high T_g (reactions N8–11 from table 3), or (ii) the local conservation of 1:2 stoichiometric ratio of C and O atoms, that is assumed in experiments for the quantification of the O atom Raman cross section [24]. Despite the simplifications in the fluid model for the chemistry and the gas flow, figures 4 and 5 show that calculations are overall in good agreement with Raman measurements. In particular, although the calculated peak T_g reaches a maximum of about 7200 K at 150 mbar, C atom mole fractions are always negligible. This result is also in agreement with calculations by Sun *et al* [29], where C atom mole fractions do not exceed values of 0.02 in similar conditions. Nevertheless, as discussed

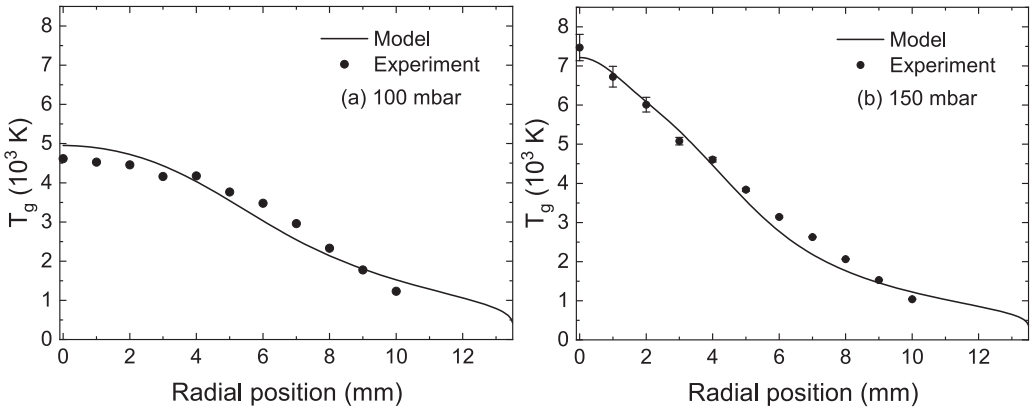

Figure 4. Measured [24] (dots) and calculated (solid line) gas temperature along the tube radius, at (a) 100 mbar and (b) 150 mbar.

in subsection 4.3, the presence of C and O atoms is fundamental for electron production through associative ionization, in the core of a CO_2 contracted plasma. Another assumption taken in the 1D model is that electronically excited states are negligible. Although these species can be important in pulsed MW conditions [97], there is no experimental evidence for a significant presence of those excited states in CW conditions that could potentially invalidate present measurements or calculations [24].

The main reaction rates for thermal dissociation of CO_2 (i.e. reverse of reactions N3–7 from table 3) calculated from the model are shown in figures 6(a) and (b) for the 100 mbar and 150 mbar cases, respectively. In both conditions, the CO_2 dissociation is mostly due to collisions with neutral species, through the following reactions (N3–5):

$$CO_2 + M \rightarrow O + CO + M,$$

where $M = CO_2$, CO, and O_2. The produced atomic oxygen atoms lead to further dissociation of CO_2 through the reaction (N6):

$$CO_2 + O \rightarrow O_2 + CO.$$

These reactions are enhanced by the high gas temperature [10, 29]. Note that, even for the case at 100 mbar, the rate of electron-impact dissociation of CO_2 is at least two orders of magnitude lower than the ones for thermal dissociation. Indeed, electron-impact dissociation of CO_2 is found to be dominant only at lower pressures, around 60 mbar [10, 23]. For radial positions larger than 5 mm, towards the edge of the tube, the CO_2 content increases due to a drop in the gas temperature. Reaction rates for CO_2 dissociation are largely reduced at lower T_g.

To summarize, for the high gas temperatures considered in this work, CO_2 dissociation is mainly driven by thermal reactions and not by electron impact reactions. Hence, in agreement with [10], experimental results of conversion and energy efficiency can be explained by considering only thermal composition and turbulent gas flow dynamics, without requiring additional vibrational non-equilibrium effects [30].

4.2. Charged species composition and electron temperature

In the previous subsection, it has been shown that CO_2 dissociation is mainly driven by collisions between neutral atoms and molecules. However, charged particle kinetics is crucial for understanding contraction phenomena in MW plasmas [33]. An increase in T_g and ionization degree in the plasma core in the contracted regime has been observed with respect to diffuse conditions [14]. Since the input power is coupled to the electrons and transferred by collisions to the heavy species, plasma contraction is strongly related to a change in the spatial distribution of electron density.

Figure 7 shows the calculated electron and ions number densities for the diffuse (100 mbar) and contracted (250 mbar) cases. The input parameters for the model are given in table 2. At 100 mbar and 250 mbar and 1000 W, the calculated neutral species mole fractions are similar to the ones shown in figure 5 (100 mbar and 150 mbar with 700 W), with a transition from a partially dissociated to a fully dissociated plasma core. In figure 7, results of the calculations have been compared with measurements of electron number densities obtained with Thomson scattering. In figure 7(a), it is shown that O_2^+ is the dominant ion. This result is in agreement with the one obtained by Wang *et al* [28] and by Viegas *et al* [23], where O_2^+ has been found to be the dominant ion in the discharge. At 100 mbar, O_2^+ is mainly produced by ionic conversion of O^+ (i.e. reaction I10 in table 5) and CO_2^+ (I1), that is

$$CO_2 + O^+ \rightarrow CO + O_2^+,$$

and

$$O + CO_2^+ \rightarrow CO + O_2^+,$$

respectively. Note that ionic conversion tendentiously leads to the formation of ions with lower ionization potential than the reactants [23]. Excellent agreement can be observed between measured and calculated electron number densities for the 100 mbar case for the first 3 mm along the tube radius, within the experimental errors. The transition from diffuse to contracted regime is characterized by an increase in the peak electron number density, from around 3.5×10^{18} m^{-3} at 100 mbar (figure 7(a)) to 3.0×10^{19} m^{-3} at 250 mbar (figure 7(b)). Moreover, as opposed to the diffuse case, results of the model

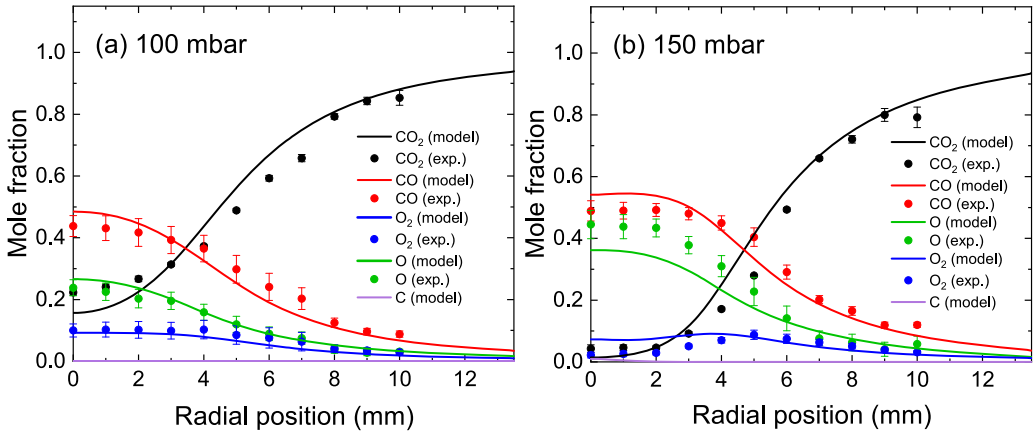

Figure 5. Measured [24] (dots) and calculated (solid line) mole fractions of the main neutral species along the tube radius, at (a) 100 mbar and (b) 150 mbar.

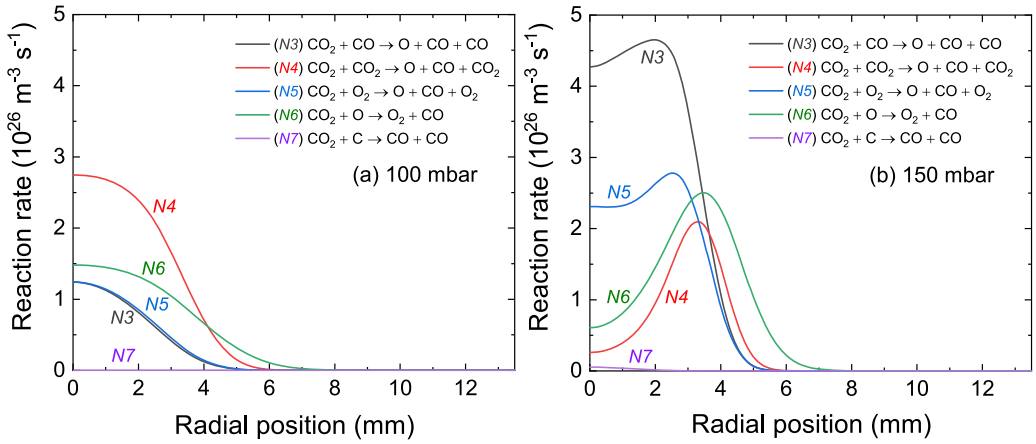

Figure 6. Thermal dissociation rates for CO_2 as a function of the radial position, at (a) 100 mbar and (b) 150 mbar.

at 250 mbar point out that the plasma in contracted regime is not composed by a single ionic species, but multiple ions are formed, namely O_2^+, O^+, and CO^+, with comparable number densities. Specifically, two spatial regions along the tube radius can be identified in the contracted regime: (i) the inner region, within 1 mm from the center, in which O^+ and O_2^+ ions are dominant and an important increase of C^+ and CO^+ number densities can be observed, compared to the 100 mbar case, and (ii) the outer region, from 1 mm up to the inner wall of the tube, where the dominant ion is again O_2^+ and, as a consequence of quasi-neutrality, this ion sets the electron number density calculated from the model at the plasma edge. In particular, results of the model suggest that CO^+ is mainly produced by associative ionization (A2):

$$C + O \rightarrow e + CO^+,$$

whereas O^+ is mainly formed by electron-impact ionization of O-atoms (E11)

$$e + O \rightarrow e + e + O^+,$$

and ionic conversion (I11)

$$O + CO_2^+ \rightarrow CO_2 + O^+.$$

In other words, collisions of O atoms with charged and neutral species determine the electron number density profile in the contracted regime.

The model under use takes a profile of power density as input, with a Gaussian shape with FWHM defined from the measured atomic oxygen emission intensity ($O(3p\ ^5P) \rightarrow O(3s\ ^5S)$). Indeed, it is assumed that atomic oxygen emission intensity, electron density and power density follow the same radial profile. As such, it is relevant to compare the measured and simulated radial profiles of electron density with the assumption based on atomic oxygen emission intensity. The normalized radial profiles of intensity measured from atomic oxygen emission and of calculated electron number density are shown in figures 8(a) and (b) from the 100 mbar and 250 mbar cases, respectively.

At 100 mbar, the normalized profile of electron number density is broader than the emission intensity profile, whereas, at 250 mbar, the normalized electron number density and emission intensity profile overlap. This can be explained by the fact that optical contraction occurs at 100 mbar, when the plasma is not fully contracted. Moreover, at 100 mbar, the radial gradient

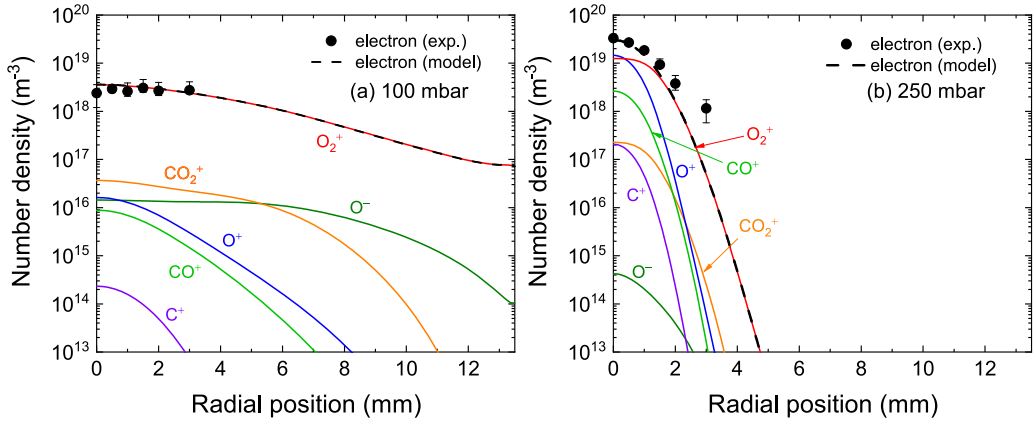

Figure 7. Measured [25] (dots) electron number densities and calculated (lines) electron and ions number densities, at (a) 100 mbar and (b) 250 mbar.

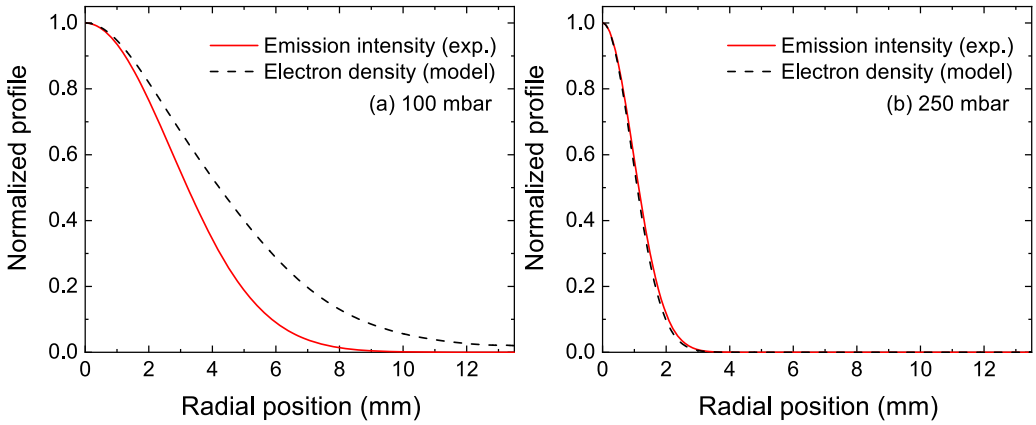

Figure 8. Measured intensity profile from atomic oxygen emission (O(3p ^{5}P) $\rightarrow$ O(3s ^{5}S)) (solid line) and calculated electron density profile (dashed line) at (a) 100 mbar and (b) 250 mbar. The profiles have been normalized to one in correspondence to the peak, at $r = 0$.

of O-atoms mole fraction is comparable to the radial gradient of the electron number density profile (figures 5(a) and 7(a)), whereas, at 250 mbar, the O-atoms mole fraction is almost radially homogeneous in the region of high n_e. This result is in agreement with the ones obtained by Viegas *et al* [38], where the optical contraction phenomenon has been predicted for gas pressures below 150 mbar and this phenomenon has been attributed to the inhomogeneous O-atoms mole fractions radial profile.

The change of ionic composition in the plasma core with pressure is shown in figure 9, where an overview of the peak electron number density measured and calculated at different pressures in the plasma core, from 100 mbar to 400 mbar, is presented. The peak number densities for the dominant ions calculated from the model have been plotted in the graph, as well. Specifically, the model reproduces the increase in electron number density in the plasma core with pressure, that is associated with contraction of CO_2 MW plasmas at 1000 W. Correspondingly, the measured ionization degree (n_e/n) in the plasma core increases from 2.5×10^{-5} at 100 mbar to 2×10^{-4} at 400 mbar. Discrepancies exceeding experimental errors can be observed for the 400 mbar case, probably due to an underestimation of the absorbed MW power density used as input to the model. The sensitivity of the calculated n_e with the input $MWPD_{inp}(0)$ is quantified in subsection 4.4. Note that, as pressure increases from 100 mbar to 400 mbar, a change in the ionic composition of the plasma core has been observed in the model, with significantly increasing number densities of O^+ and CO^+. The number density of the negative ion O^- is always below 10^{17} m^{-3}, thus this ion is negligible compared to positive ions, mainly due to detachment processes (reactions I21–24 in table 5). Moreover, for pressures above 200 mbar, O^+ is the dominant ion in the plasma core. Thus, from this study, it appears that the contraction phenomenon in CO_2 MW plasmas is related to the formation of atomic ionic species in the plasma core. This result is in agreement with the study by Viegas *et al* [23], where the importance of ion composition for CO_2 MW plasma contraction has been studied with a 0D model.

Diffuse and contracted plasmas are also characterized by different electron temperatures. In particular, radial profiles of calculated and measured T_e at 100 mbar and 250 mbar are shown in figures 10(a) and (b), respectively. Measurements are limited within a 3 mm range from the center of the tube, as the Thomson signal is reduced by a lower electron number density and by an increase in CO_2 number density at outer

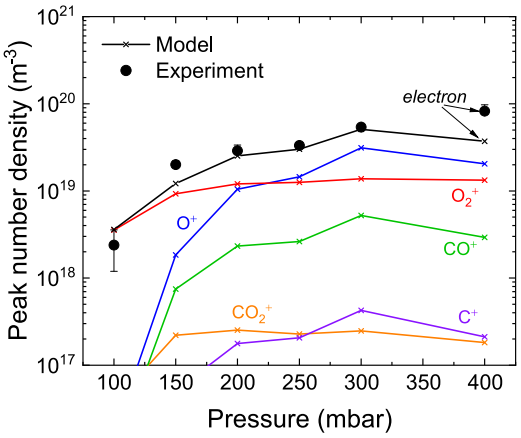

Figure 9. Measured electron number density [25] (dots) and calculated electron and ion number densities (lines) in the center of the tube, for different pressures.

positions along the tube radius. Calculated electron temperatures (T_e) are derived from MCF as $T_e = 2\langle\epsilon\rangle/3$, where $\langle\epsilon\rangle$ is the electron mean energy.

On the one hand, the diffuse case (figure 10(a)) shows that T_e is constant within the first 3 mm along the tube radius. For this case, measurements and 1D model results are in good agreement, within the experimental errors. On the other hand, T_e is found to increase outwards for the contracted case (figure 10(b)), from a value of 1 eV in the center of the tube to around 2 eV at 3 mm. This increase is not reproduced by the model, where a concave T_e profile has been obtained. Note that a similar increase in T_e near the wall has been measured also by Carbone *et al* [98] with Thomson scattering in contracted MW plasmas operated with argon at intermediate pressures, from 20 mbar to 88 mbar. This trend has been explained by Jimenez-Diaz *et al* [99] as a consequence of the non-homogeneity of the ionization frequency across the radius, using a 2D fluid model. However, note that the model by Jimenez-Diaz *et al* [99] considers Maxwell–Boltzmann EEDFs in the calculations. This assumption has been demonstrated to not be accurate for argon MW plasmas by Ridenti *et al* [34], where the increase in T_e has been explained as a result of an implicit Maxwellian assumption for the EEDF in Thomson scattering. In [34], a Thomson temperature ($T_{e,Th}$) is defined as the temperature obtained by fitting the non-equilibrium EEDF with a Maxwell–Boltzmann distribution in the 0–2 eV energy range. As the low-energy part of the distribution (i.e. the head of the EEDF) gives most of the contribution to the measured Thomson signal, the $T_{e,Th}$ defined in this way is comparable with the electron temperature measured by Thomson scattering. Following the idea by Ridenti *et al* [34], the $T_{e,Th}$ values derived from the corresponding non-equilibrium EEDFs are shown in figure 10, for the cases at 100 mbar and 250 mbar. In particular, for the 100 mbar case (figure 10(a)), differences between calculated T_e and $T_{e,Th}$ are within 15%. At 250 mbar (figure 10(b)), the $T_{e,Th}$ is found to be in good agreement with experimental values, as the outward increase of measured T_e has been reproduced. Therefore, the measurement of convex T_e at 250 mbar (figure 10(b)) are attributed to the Maxwellian assumption implicit in the Thomson scattering diagnostic and not to a higher mean electron energy. Note that results presented in this section have been obtained without the inclusion of electron–electron collisions. Indeed, with the addition of self-collisions of electrons in the MCF code, the EEDF is expected to approach the Maxwell–Boltzmann equilibrium distribution [100]. The importance of this effect would be larger in the center of the tube than at the edge, since the ionization degree (n_e/n) is highest at $r = 0$. Nevertheless, EEDF calculations using the two-term solver BOLSIG+ [101, 102] confirmed that the addition of self-collisions of electrons do not have an appreciable effect on the previous results. In fact, rate coefficients for electron impact ionization of CO and O obtained including electron–electron collisions in BOLSIG+ are within 5% with respect to the ones obtained by the same solver by neglecting this contribution. Therefore, from the present considerations, it is expected that these collisions would not change the results in this section by more than a few percent, although this mechanism would contribute to increase ionization in the core, and thus would be an extra contribution to contraction.

Central E/n values calculated at different pressures are shown in figure 11, where $E = E_0/\sqrt{2}$ is the mean square value of the MW field, with E_0 the maximum amplitude of the field in the course of a period oscillation [62]. Figure 11 shows that E/n in the plasma core is decreasing with increasing pressure. The same result has been reported by Viegas *et al* [23], Pietanza *et al* [22], and Groen *et al* [103]. In particular, Pietanza *et al* [22] obtained lower E/n values than the ones calculated in this work, in the range 48–50 Td and 25–42 Td for the 100 mbar and 250 mbar cases, respectively. Nevertheless, their calculated peak electron number densities are close to the ones reported in this work, within a few percent. The main differences between the present study and the one by Pietanza *et al* [22] are related to input parameters, different dimensionality of the models, gas temperature and mass transport that are considered in the models. In fact, in [22], a 0D model has been used in which the MW power density has been assumed to be uniform in the discharge, whereas a radial profile has been considered in this work (equation (26)). Moreover, the peak power densities values in [22] are lower than the ones used here. In Viegas *et al* [23], it has been found that E/n decreases from around 80 Td at 100 mbar to 67 Td at 300 mbar. However, in the same work, it has also been shown that this parameter is subjected to large uncertainties depending on mass transport and input gas temperature. Moreover, as described in subsection 3.5, different electron impact cross sections sets have been used by Pietanza *et al* [22] and by Viegas *et al* [23], with respect to this work. The central E/n values obtained in this work are in good agreement with estimations by Groen *et al* [103]. However, note that different methods have been used for calculations of E/n. On the one hand, in [103], a 3D electromagnetic model has been used, where the field has been obtained by varying the MW power through impedance matching. On the other hand, in this work, the field has been considered as an internal parameter of the simulation

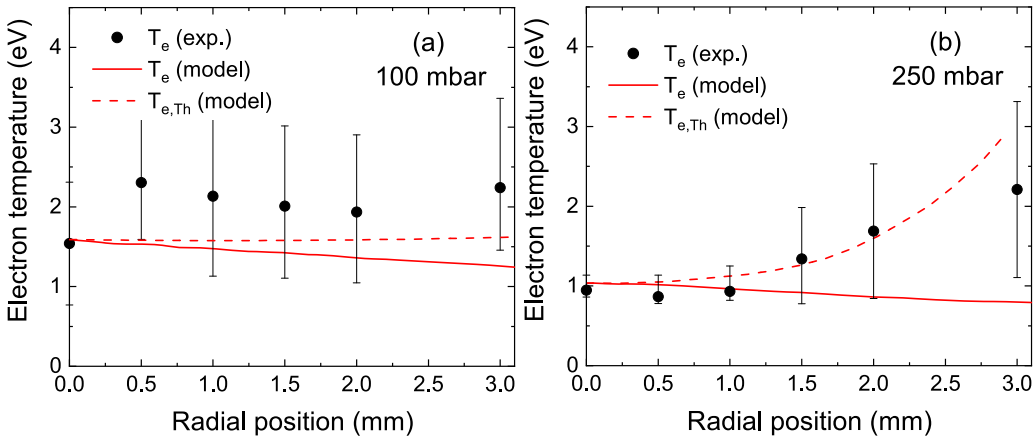

Figure 10. Radial profile of measured electron temperature from Thomson scattering [25] (dots), calculated electron temperature as $T_e = 2\langle\epsilon\rangle/3$ (solid line), and Thomson temperature $T_{e,Th}$ derived from fitting of the EEDFs with a Maxwell–Boltzmann distribution in the 0–2 eV energy interval (dashed line), for (a) 100 mbar and (b) the 250 mbar.

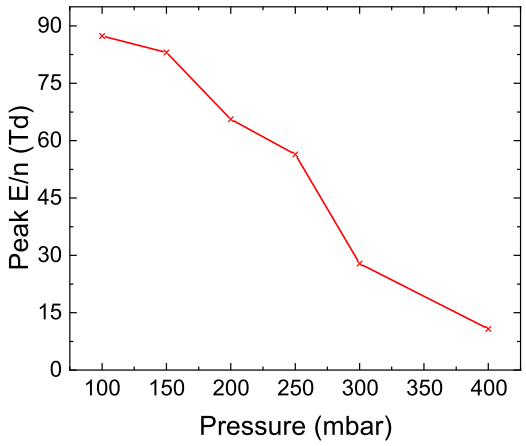

Figure 11. Calculated mean square values of the reduced electric field in the center of the tube, for different pressures.

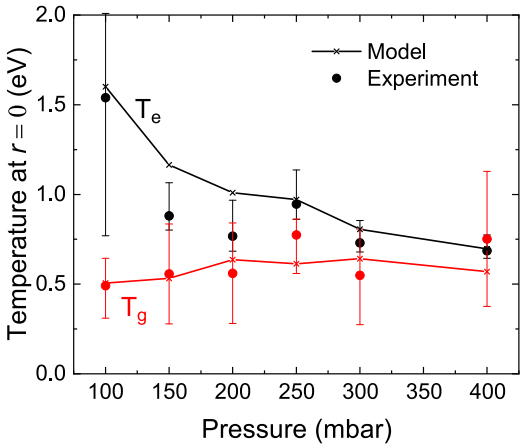

Figure 12. Measured [25] (dots) and calculated (lines) electron temperatures (black) and gas temperatures (red) in the center of the tube, as a function of pressure.

and has been obtained by an iterative procedure under the condition that the plasma power losses adjust to compensate for the total MW deposited power, as described in subsection 3.4.

Measured and calculated T_e and T_g at $r = 0$ are shown in figure 12, for different pressures from 100 mbar to 400 mbar. Opposite trends are found for T_e and T_g with increasing pressure. In particular, as a result of the decrease in the central E/n (figure 11) with pressure, T_e decreases from 1.5 eV at 100 mbar to 0.6 eV at 400 mbar, whereas T_g increases slightly from 0.5 eV to 0.6 eV. Note that this equilibration is not predicted by the 0D model results by Viegas *et al* [23] and Pietanza *et al* [22], where T_e has been found to increase with increasing pressure. Sources for these discrepancies are discussed in subsection 4.4.

To summarize, the present comparison of measurements and calculations of discharge parameters in CO_2 MW discharges showed that (i) the diffuse regime is characterized by a single dominant ion species (O_2^+) and $T_e > T_g$ in the plasma core, (ii) the contracted regime is characterized by a multi-ionic composition, with higher values of O^+ ion number density than the contracted case and $T_e \approx T_g$ in the plasma core for $p_g > 200$ mbar.

4.3. Insight into plasma contraction from model results

This section investigates the charged particle kinetics and highlights the main chemical reactions leading to the results in the previous section. In particular, in figure 9, it has been shown that the peak electron number density increases from 2.5×10^{18} m^{-3} at 100 mbar to around 3.0×10^{19} m^{-3} at 250 mbar. As described by Zhong *et al* [104, 105], it is expected that higher n_e would require higher T_e values in the center of the tube, in order to sustain the discharge in the contracted regime. However, in figure 12, it is shown that the electron temperature at $r = 0$ decreases from 1.5 eV to 1.0 eV, as the pressure increases from 100 mbar to 250 mbar. In order to investigate the mechanisms leading to this decrease in T_e, the main electron production rates are plotted in figure 13. At 100 mbar (figure 13(a)), the discharge is mostly sustained by electron detachment from CO and O^- (reaction I21 in table 5) and by electron impact ionization of CO and O in the center of the tube (reactions E6 and E11 in table 4). At 250 mbar (figure 13(b)), the rates of associative ionization for electron production are several orders of magnitude larger than those

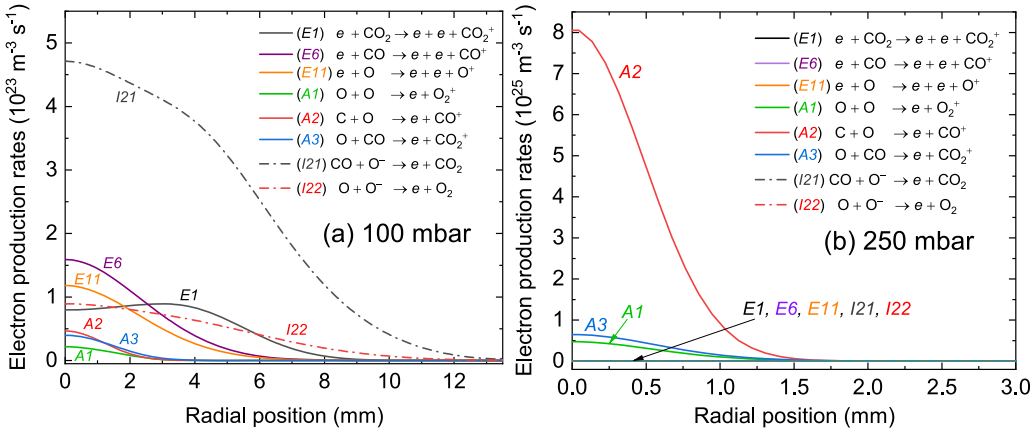

Figure 13. Reaction rates for the main electron production mechanisms calculated at (a) 100 mbar and (b) 250 mbar, as a function of the radial coordinate.

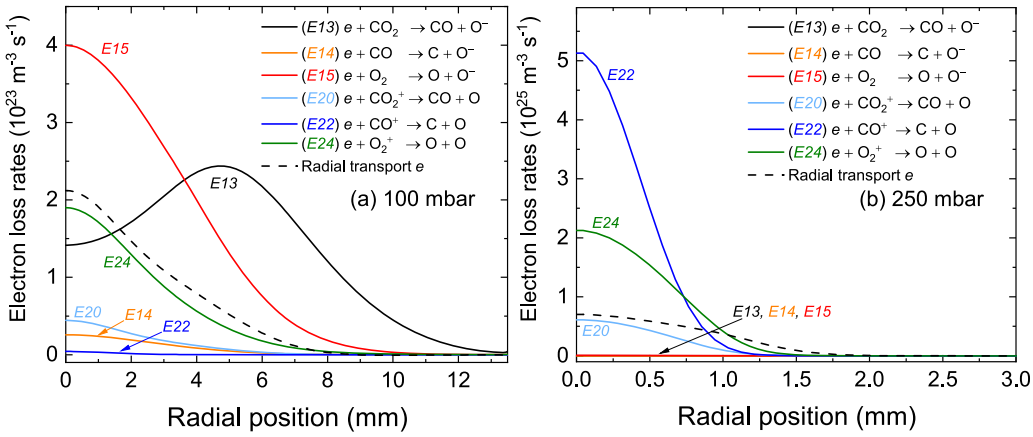

Figure 14. Main electron loss rates calculated at (a) 100 mbar and (b) 250 mbar, as a function of the radial coordinate.

for electron-impact ionization and electron detachment. In particular, the dominant ionization reaction is the one producing CO^+ (reaction A2 of table 6):

$$C + O \rightarrow e + CO^+.$$

Moreover, note that models neglecting associative ionization reactions cannot predict accurate values of T_e in both diffuse and contracted regimes. For example, the work by Pietanza *et al* [22] reports T_e values in the range 0.86–1.20 eV at 100 mbar and 1.20–1.46 eV at 250 mbar, that are not compatible with the present experimental measurements. Indeed, without associative ionization mechanisms, the only source for electron production included in that model is electron impact ionization, whose rate increases at higher T_e values. Thus, it is possible to conclude that, as a consequence of associative ionization, higher electron production rates can be achieved in contracted conditions, without the need of higher T_e values, with respect to the diffuse case.

The main loss rates for electrons at 100 mbar and 250 mbar are shown in figures 14(a) and (b), respectively. Figure 14 shows that diffuse and contracted regimes are characterized by a different electron kinetics. In particular, at 100 mbar (figure 14(a)), electron attachment to O_2 (E15) is the dominant electron loss mechanism in the center of the tube (within 4 mm radius), whereas electron attachment to CO_2 (E13) is the dominant electron loss mechanisms towards the edge. At 250 mbar (figure 14(b)), electron loss rates are dominated by dissociative recombination of electrons with CO^+ (E22) and O_2^+ (E24) ions. Moreover, as pressure increases, attachment is suppressed. This result is in agreement with the work by Wolf *et al* [15] and by Fridman and Kennedy [106] stating that, in the contracted regime, CO_2 discharges are controlled by electron–ion recombination. Moreover, on the one hand, at 100 mbar, the radial electron diffusion rate is of the same order of magnitude as the electron–ion recombination rate. On the other hand, at 250 mbar, the radial electron diffusion rate in the center of the tube is a factor 5 lower than the rate of dissociative recombination of electrons with CO^+. Hence, radial diffusion of electrons is suppressed at high pressures.

To summarize, the following considerations about contraction in CO_2 MW plasmas can be deduced. At higher pressures, the gas temperature increases in the plasma core. Hence, associative ionization of C and O atoms becomes the dominant mechanism for electron production. This mechanism leads to increasing peak n_e, without the need of increasing T_e at $r = 0$, hence generating a self-reinforcing cycle between heating and increasing n_e in the plasma core. As a result of a higher T_g

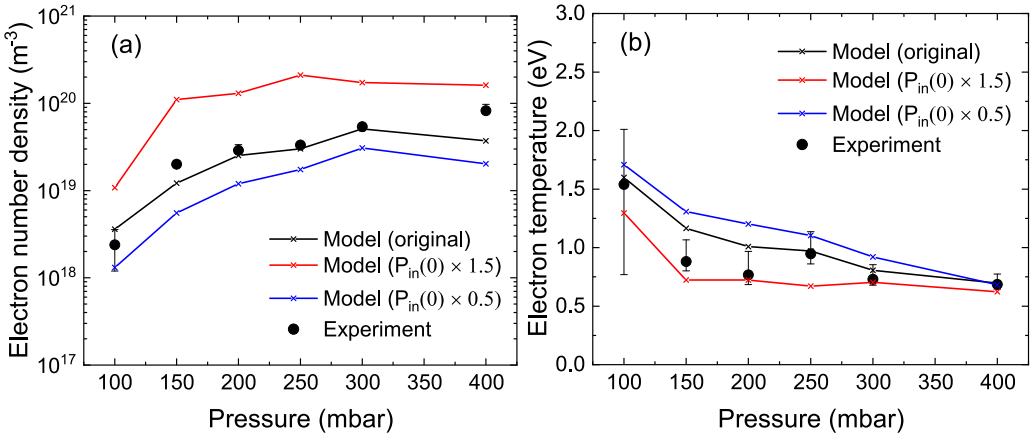

Figure 15. Measured (dots) and calculated (lines) (a) electron number densities and (b) electron temperatures at $r = 0$, as a function of pressure. Effect of uncertainties in the peak absorbed MW power density ($P_{in}(0)$) is investigated by comparing results of the original model (black line), with the ones obtained by increasing (red line) or decreasing (blue line) $P_{in}(0)$ by 50%.

at $r = 0$ with increasing pressure, a change of composition occurs in the plasma core. Hence, the plasma becomes fully dissociated into CO and O in the center and molecular ions dissociate into atomic ones. In particular, for pressures above 200 mbar at 1000 W, O_2^+ is no longer the most abundant ion in the center, in favour of O^+. The transition in dominant ion has also been noted by Martinez *et al* [33] and by Ridenti *et al* [34], for MW plasmas operated in argon at atmospheric pressure. Moreover, the importance of the change in neutral and charged species composition for discharge contraction has also been highlighted by Viegas *et al* [23]. However, in [23], it is hypothesised that the change of electron impact ionization rate coefficients with composition is a key mechanism for the increase of n_e in the plasma core. This hypothesis is excluded by the results of this work, as associative ionization rates are dominant at high pressure, with respect to electron impact ionization rates. From this study, it is possible to conclude that non-uniform gas heating along the tube radius is the responsible mechanism for discharge contraction in CO_2. The same mechanism has been hypothesised by Viegas *et al* [23] for CO_2 MW plasmas. However, in [23], radial gradients in gas temperature and species mole fractions have not been taken into account, as the focus of that work was the simulations of the main processes in the plasma core using a 0D plasma chemistry model. Indeed, due to gradients in the radial profile of T_g, molecular ions are efficiently dissociated in the center of CO_2 MW plasmas, therefore reducing the number of molecular ions for dissociative recombination [33]. Additionally, as pressure increases, radial transport of electrons and attachment of electrons to O_2 molecules are suppressed. Therefore, in contracted regime, charged species are not easily transported towards the edge of the tube, as in the diffuse case, and the radial extension of the plasma is uniquely determined by a balance between electron–ion recombination and associative ionization.

4.4. Possible sources of uncertainties

4.4.1. Effect of absorbed microwave power density. The MW power density profile ($P_{in}(r)$) used as input to the model (equation (19)) has been estimated from experimental measurements of the 777 nm spectral line emission profile of atomic oxygen [14]. The estimation of this parameter from the emission intensity profile is based on several assumptions [38]. Specifically, (i) a Gaussian profile of emission intensity, electron number density and MW power density has been assumed, (ii) the gas composition and reduced electric field have been considered to be radially homogeneous, and (iii) proportionality between emission intensity and electron density has been assumed. Since these assumptions are not fully met for the conditions under investigation (see figure 8(a)), large uncertainties are associated to $P_{in}(r)$, up to 50% [23, 38]. In order to investigate the effect of these uncertainties on the model results, calculations have been performed increasing $P_{in}(0)$ by 50%, as well as decreasing this parameter by the same percentage. Since volume integrated MW power density is conserved, the axial and radial FWHM are multiplied by a factor 1.26 for a 50% decrease in $P_{in}(0)$ or by a factor 0.79 for a 50% increase in $P_{in}(0)$. Hence, the total (volume integrated) input MW power is unchanged. Results of the calculations of n_e and T_e at $r = 0$ as a function of pressure are shown in figures 15(a) and (b), respectively.

For a 50% increase in $P_{in}(0)$ with respect to the original value, n_e increases by a factor between 3 and 10. In fact, higher values of $P_{in}(0)$ lead to higher peak T_g through equation (19) and, in turn, to higher rates of associative ionization (i.e. reactions A1–3 in table 6), that are the main mechanisms for electron production. Conversely, a 50% decrease in $P_{in}(0)$ results in lower ionization rates from reactions A1–3, which in turn leads to lower electron number densities than the experimental ones. Nevertheless, the difference between n_e obtained from the original model and the ones obtained by lowering $P_{in}(0)$ is not a factor 10 as before, but only a factor 3. Figure 15(b) shows that lower T_e values are obtained by increasing $P_{in}(0)$ by 50%. Indeed, for higher $P_{in}(0)$ associative ionization becomes increasingly important. Hence, a lower T_e value is sufficient to maintain the discharge and match $P_{in}(r)$ in the model. Therefore, it is possible to conclude that a change in the input peak value of the MW power density drastically affects the

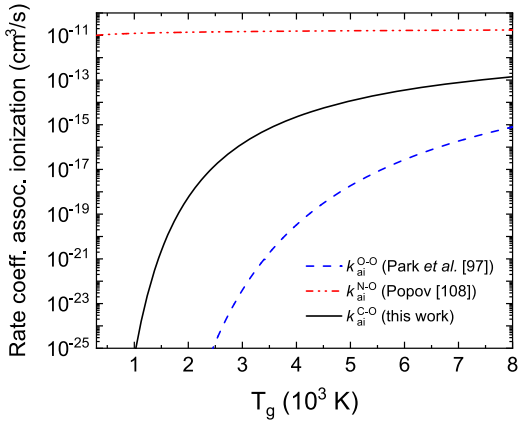

Figure 16. Rate coefficient for associative ionization of C + O (k_{ai}^{C-O}) used in this work (solid black line), for O + O (k_{ai}^{O-O}) reported by Park *et al* [96] (dashed blue line), and for N + O (k_{ai}^{N-O}) reported by Popov [107] (dashed–dotted red line).

calculations of T_g and, in turn, of n_e. Moreover, simulation results point out that the original input $P_{in}(r)$ is the most appropriate for reproducing experimental values of n_e, for all the conditions considered in this work.

Changing the value of $P_{in}(0)$ directly affects E/n calculations and the T_e values that are computed from MCF. In order to avoid that uncertainties in $P_{in}(0)$ affect model results, a possible alternative solution is to take as input a radial n_e profile, instead of $P_{in}(r)$. This procedure has been adopted by Viegas *et al* [38], where a 1D fluid model has been used to study optical contraction in CO_2 MW plasmas. Nevertheless, note that measurements of n_e are limited to radial positions within 3 mm from the center of the tube and accurate radial profiles of electron density are not directly accessible from experiments. Therefore, in [38], a collisional-radiative model for O-atoms has been coupled to the fluid model, in order to calculate the electron properties of the discharge through an iterative procedure. Another possibility would be to include the solution of Maxwell's equations for the electromagnetic field and a momentum balance equation for the electrons. As such, the model would become fully self-consistent and the profile of the MW absorbed power density could be directly computed from the Ohmic heating equation [63]. However, note that the forward-vortex reactor used at DIFFER breaks the axial symmetry due to the rectangular MW cavity. Hence, it would be better to use 2D or 3D self-consistent plasma models in this case, in order to better reproduce the experimental set up.

4.4.2. Effect of associative ionization. As mentioned in the previous subsection, associative ionization from the interactions between C and O atoms is the dominant mechanism for electron production in the contracted CO_2 plasma. However, large uncertainties are associated with the rate coefficient for this process. The following three different expressions for associative ionization rate coefficients have been found in literature:

- In this work, the rate coefficient for the reaction C + O → CO^+ + e has been assumed to be equal to

$$k_{ai}^{C-O} = 8.78 \times 10^{-12} \exp\left(-\frac{33\,100}{T_g[K]}\right) \text{ cm}^3 \text{ s}^{-1}, \quad (39)$$

where T_g[K] is the gas temperature in kelvin. The pre-exponential factor and the activation energy in equation (39) above have been taken from the work by Park *et al* for the same reaction [94]. However, as recommended in [96], the pre-exponential power has been assumed equal to zero (see subsection 3.5). Note that the expression of k_{ai}^{C-O} assumed by Park *et al* [94] is derived from the N + O associative ionization reaction that has similar activation energy and pre-exponential factor. In fact, associative ionization involves the interaction of excited C and O atoms [107] and this effective rate coefficient considers C and O atoms as a whole, with excited states populated according to a Boltzmann distribution. This formulation is consistent with the assumptions made in the model., where a Boltzmann population is assumed for the electronically excited states.

- In [96], Park report an expression for the rate coefficient for associative ionization between O atoms (i.e. O + O → O_2^+ + e)

$$k_{ai}^{O-O} = 1.18 \times 10^{-21} T_g^{2.7} \exp\left(-\frac{80\,600}{T_g[K]}\right) \text{ cm}^3 \text{ s}^{-1}. \quad (40)$$

Note that this rate coefficient has been used in the model by Viegas *et al* [23] for both O + O and C + O mechanisms.

- In [107], Popov reports an expression for associative ionization involving N-atoms, that is N + O → NO^+ + e. The rate coefficient for this process has been assumed equal to

$$k_{ai}^{N-O} = 1 \times 10^{-11} \left(\frac{T_g[K]}{300}\right)^{1/6} \text{ cm}^3 \text{ s}^{-1}. \quad (41)$$

Since the C + O associative ionization reaction and N + O reaction have comparable activation energies [94], it is common in chemistry models to assume that the rate coefficient for the C + O reaction is equal to the one for the N + O reaction. We should notice that, in the work by Popov [107], the rate constant for associative ionization of N + O involves exclusively electronically excited N-atoms. This is why this rate constant is so high and has a very weak dependence on the gas temperature. Hence, it should be applied only in models solving the mass balance equation for separate electronically excited states, which is not the case in this work.

Figure 16 shows a plot of these rate coefficients as a function of the gas temperature, in the range 300–8000 K. k_{ai}^{O-O} is lower than k_{ai}^{C-O} by about two orders of magnitude at 7000 K, due to the higher activation energy associated to the O + O reaction than to the C + O one. Furthermore, k_{ai}^{N-O} is almost constant in the gas temperature range considered and it is more than two orders of magnitude higher than k_{ai}^{C-O}, at 7000 K. Since C + O associative ionization is the main mechanism for

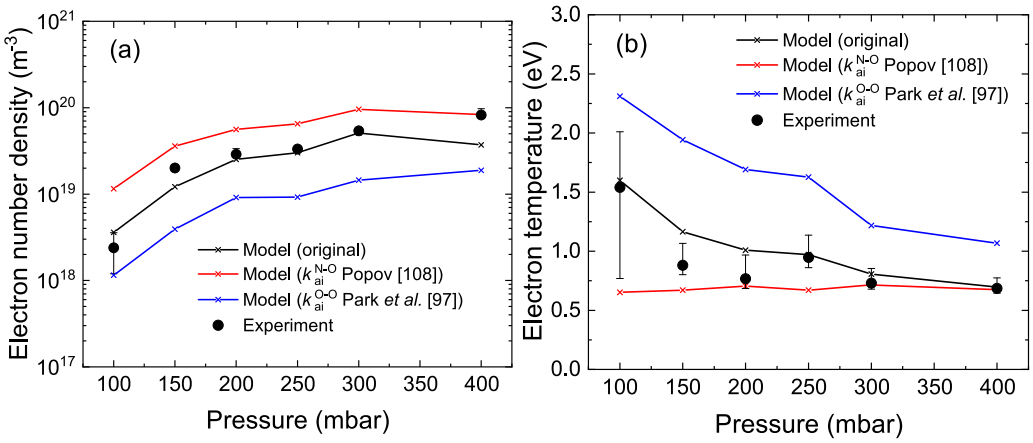

Figure 17. Measured (dots) and calculated (lines) (a) electron number densities and (b) electron temperatures at $r = 0$ as a function of pressure. Effect of uncertainties in the associative ionization rate coefficient for C + O is investigated by comparing results of the original model (black line), with the ones obtained by using different expression for this rate coefficient, as given by Park [96] (blue line) and by Popov [107] (red line).

electron production, it is expected that the use of a very different rate coefficient for this process would lead to high deviations in n_e and T_e. Figures 17(a) and 17(b) show results of the model for n_e and T_e at $r = 0$, when different rate coefficients from equations (40) and (41) are used instead of equation (39), that is the one adopted in the original model. As expected, the use of k_{ai}^{O-O} instead of k_{ai}^{C-O} leads to lower n_e values than the ones calculated from the original model, due to the fact that k_{ai}^{O-O} is much lower than k_{ai}^{C-O}. At the same time, higher T_e values than the measured ones have been obtained, by about 1.0 eV. Similar values have been obtained by Viegas *et al* [23], where electron temperatures in the range 1.8–2.0 eV, for pressures between 100 mbar and 300 mbar, have been obtained. Indeed, in [23], k_{ai}^{O-O} has been used also for the C + O associative ionization reaction and this assumption leads to large deviations from experimental measurements. Moreover, note that the 0D model results in [23] predict an increase in T_e with pressure, that is in contrast with the Thomson scattering measurements reported in this work. These discrepancies are due to the fact that, in [23], both n_e and T_g from experimental measurements have been used as input for the model. In particular, the peak T_g values used in the 0D model are lower than the ones calculated here, by about 800 K. Hence, lower associative ionization rates than the ones in this work have been obtained in [23].

Assuming that the associative ionization rate coefficient for the C + O reaction is the same as the one for the N + O reaction of Popov [107], higher peak n_e values have been obtained (figure 17(a)), with respect to the ones calculated with the original model. In fact, the rate coefficient for associative ionization reported by Popov [107] (equation (41)) is exceedingly higher than the one used in this work (equation (39)), thus higher electron production rates have been obtained. Figure 17(b) shows also that T_e is largely affected by using k_{ai}^{N-O}, instead of k_{ai}^{C--O}. In particular, T_e is almost constant with pressure when using the rate coefficient by Popov [107] in the model. This result is expected, since k_{ai}^{N-O} is almost constant in the range 300–8000 K (figure 16), hence this associative ionization mechanism would be the dominant electron production rate, even at lower pressures that are typical of diffuse plasmas.

To summarize, calculations of n_e and T_e in CO_2 MW discharges are largely affected by the choice of associative ionization rate coefficients. Indeed, by changing the rate coefficient for associative ionization from C and O atoms, discrepancies between calculations and measurements exceeding experimental errors have been found. Therefore, the present results point out that future plasma chemistry models for plasmas featuring gas temperatures of the order of thousands K should take into account accurate expressions for associative ionization rate constants. These results show that the expressions for rate constants of associative ionization reported in table 6 are the ones giving the best agreement between calculations and experiments. However, further validation of associative ionization rate coefficients against shock-tube measurements at high T_g is needed.

5. Conclusions

A vortex-stabilized CO_2 MW plasma at a fixed MW input power of 700 W and 1000 W and different pressures, from 100 mbar to 400 mbar, has been studied through comparisons between simulations and experiments. For this purpose, a 1D radial fluid model that takes into account accurate calculations of chemical rates, thermodynamic, transport and radiation quantities has been developed. Moreover, the fluid model has been coupled to a MCF code for electron kinetics. Neutral species mole fractions, gas temperature, electron number density and electron temperature, calculated from the model, have been validated against spatially-resolved measurements obtained by means of Thomson and Raman laser scattering diagnostics.

Measurements and simulations show, with good agreement between them, that, as pressure increases, T_g increases in the plasma core from 4900 K to 7200 K, hence the neutral species composition becomes increasingly more dissociated

due to thermal chemistry. Both n_e and n_e/n increase in the plasma core with pressure, from 2×10^{19} m^{-3} at 100 mbar to 6×10^{19} m^{-3} at 400 mbar and from 2.5×10^{-5} at 100 mbar to 2×10^{-4} at 400 mbar, respectively. Moreover, T_e decreases from 1.5 eV to 0.6 eV in the plasma core, with increasing pressure.

Results of the model show that, as pressure increases above 100 mbar, sharper radial gas temperature gradients are formed. Moreover, at higher pressures, radial diffusion of electrons and electron attachment to CO_2 and O_2 molecules are largely suppressed. Hence, for pressures above 100 mbar, charge losses are uniquely determined by electron recombination with CO^+ and O_2^+ ions. As a consequence of the high T_g, molecular ions tend to dissociate into atomic species in the center of the tube, thus the role of electron–ion recombination decreases in the core, while being maintained at the edges. The present results are in agreement with previous studies by Martinez *et al* [33], Ridenti *et al* [34], and Viegas *et al* [23] confirming that plasma contraction can be explained by non-uniform gas heating. In addition, this work highlights the role of associative ionization as dominant electron production mechanism in the plasma core, as pressure increases above 100 mbar. This mechanism is favoured by the high T_g and by the consequent dissociation of CO into C and O atoms and it leads to an increase of core n_e and a decrease of core T_e, with increasing pressure. Thus, a self-reinforcing cycle between n_e and heating in the core is established. Results of this work confirm the hypothesis by Wolf *et al* [15] of the importance of the coupling between thermal-ionization instability and plasma chemical kinetics in driving contraction in CO_2 MW plasmas. Nevertheless, as opposed to the conventional thermal-ionization instability based on electron impact ionization described by Zhong *et al* [104, 105], here the instability is driven by associative ionization reactions.

This work has shown that the output of the fluid-MCF model is also largely sensitive to the choice of adjustable quantities, such as the input MW power density and associative ionization rate coefficients. In this respect, this work can be considered as a step forward with respect to 0D plasma chemistry models towards a systematic validation of multi-dimensional model results against experiments for MW discharges in CO_2.

Acknowledgments

The authors would like to thank L Baldassi from University College Roosevelt for implementation and benchmarking of thermodynamic parameters used in the fluid model. PV acknowledges support by the project LM2018097 funded by the Ministry of Education, Youth and Sports of the Czech Republic. This work is part of the Shell-NWO/FOM initiative 'Computational Sciences for Energy Research' of Shell and Chemical Sciences, Earth and Life Sciences, Physical Sciences, FOM and STW.

Data availability statement

All data that support the findings of this study are included within the article (and any supplementary files).

ORCID iDs

L Vialetto https://orcid.org/0000-0003-3802-8001
A W van de Steeg https://orcid.org/0000-0002-2976-7905
P Viegas https://orcid.org/0000-0002-3820-3300
S Longo https://orcid.org/0000-0002-5038-7659
G J van Rooij https://orcid.org/0000-0003-4795-3274
M C M van de Sanden https://orcid.org/0000-0002-4119-9971
J van Dijk https://orcid.org/0000-0001-8002-5459
P Diomede https://orcid.org/0000-0002-4523-3049

References

[1] Snoeckx R and Bogaerts A 2017 *Chem. Soc. Rev.* **46** 5805–63
[2] van Rooij G J *et al* 2015 *Faraday Discuss.* **183** 233–48
[3] Goede A P H, Bongers W A, Graswinckel M F, van de Sanden R M C M, Leins M, Kopecki J, Schulz A and Walker M 2014 *EPJ Web Conf.* **79** 01005
[4] Qin Y, Niu G, Wang X, Luo D and Duan Y 2018 *J. CO_2 Util.* **28** 283–91
[5] George A, Shen B, Craven M, Wang Y, Kang D, Wu C and Tu X 2021 *Renew. Sustain. Energy Rev.* **135** 109702
[6] Legasov V A *et al* 1978 *Dokl. Akad. Nauk* **238** 66–9
[7] Butylkin Y P, Zhivotov V K, Krasheninnikov E G, Krotov M F, Rusanov V D, Tarasov Y V and Fridman A A 1981 *Sov. Phys. Tech. Phys.* **26** 555–8
[8] Asisov R I, Fridman A A, Givotov V K, Krsheninnikov E G, Patrushev B I, Potapkin B V, Rusanov V D and Krotov M F 1981 Carbon dioxide dissociation in nonequilibrium plasma *5th Int. Symp. on Plasma Chemistry* vol 2 pp 774–9
[9] Fridman A 2008 *Plasma Chemistry* (Cambridge: Cambridge University Press)
[10] van de Steeg A, Viegas P, Silva A, Butterworth T, van Bavel A, Smits J, Diomede P, van de Sanden M and van Rooij G 2021 *ACS Energy Lett.* **6** 2876–81
[11] van den Bekerom D C M, Linares J M P, Verreycken T, van Veldhuizen E M, Nijdam S, Berden G, Bongers W A, van de Sanden M C M and van Rooij G J 2019 *Plasma Sources Sci. Technol.* **28** 055015
[12] van den Bekerom D C M, van de Steeg A, van de Sanden M C M and van Rooij G J 2020 *J. Phys. D: Appl. Phys.* **53** 054002
[13] van de Steeg A W, Butterworth T, van den Bekerom D C M, Silva A F, van de Sanden M C M and van Rooij G J 2020 *Plasma Sources Sci. Technol.* **29** 115001
[14] Wolf A J, Righart T W H, Peeters F J J, Groen P W C, van de Sanden M C M and Bongers W A 2019 *Plasma Sources Sci. Technol.* **28** 115022
[15] Wolf A J, Righart T W H, Peeters F J J, Bongers W A and van de Sanden M C M 2020 *Plasma Sources Sci. Technol.* **29** 025005
[16] D'Isa F A, Carbone E A D, Hecimovic A and Fantz U 2020 *Plasma Sources Sci. Technol.* **29** 105009
[17] Beuthe T G and Chang J-S 1997 *Japan. J. Appl. Phys.* **36** 4997–5002
[18] Kozák T and Bogaerts A 2014 *Plasma Sources Sci. Technol.* **23** 045004

[19] Koelman P, Heijkers S, Tadayon Mousavi S, Graef W, Mihailova D, Kozák T, Bogaerts A and van Dijk J 2017 *Plasma Process. Polym.* **14** 1600155

[20] Berthelot A and Bogaerts A 2017 *J. Phys. Chem.* C **121** 8236–51

[21] Vermeiren V and Bogaerts A 2020 *J. Phys. Chem.* C **124** 18401–15

[22] Pietanza L D, Colonna G and Capitelli M 2020 *Plasma Sources Sci. Technol.* **29** 035022

[23] Viegas P, Vialetto L, Wolf A J, Peeters F J J, Groen P W C, Righart T W H, Bongers W A, van de Sanden M C M and Diomede P 2020 *Plasma Sources Sci. Technol.* **29** 105014

[24] van de Steeg A W, Vialetto L, Silva A F, Peeters F J J, van den Bekerom D C M, Gatti N, Diomede P, van de Sanden M C M and van Rooij G J 2021 *Opt. Lett.* **46** 2172–5

[25] van de Steeg A W, Vialetto L, Silva A F S d, Viegas P, Diomede P, van de Sanden M C M and van Rooij G J 2022 *J. Phys. Chem. Lett.* **13** 1203–8

[26] Kotov V and Koelman P M J 2019 *Plasma Sources Sci. Technol.* **28** 095002

[27] Ponduri S, Becker M M, Welzel S, van de Sanden M C M, Loffhagen D and Engeln R 2016 *J. Appl. Phys.* **119** 093301

[28] Wang W, Berthelot A, Kolev S, Tu X and Bogaerts A 2016 *Plasma Sources Sci. Technol.* **25** 065012

[29] Sun H, Lee J, Do H, Im S-K and Soo Bak M 2017 *J. Appl. Phys.* **122** 033303

[30] Wolf A J, Peeters F J J, Groen P W C, Bongers W A and van de Sanden M C M 2020 *J. Phys. Chem.* C **124** 16806–19

[31] Golubovskii Y B, Lange H, Maiorov V A, Porokhova I A and Sushkov V P 2003 *J. Phys. D: Appl. Phys.* **36** 694–703

[32] Petrov G M and Ferreira C M 1999 *Phys. Rev.* E **59** 3571–82

[33] Martinez E C, Kabouzi Y, Makasheva K and Moisan M 2004 *Phys. Rev.* E **70** 066405

[34] Ridenti M A, Amorim J D, Pino A D, Guerra V and Petrov G 2018 *Phys. Rev.* E **97** 013201

[35] Moisan M and Pelletier J 2012 *Physics of Collisional Plasmas: Introduction to High-Frequency Discharges* (Dordrecht: Springer Science & Business Media)

[36] Vialetto L, Longo S and Diomede P 2019 *Plasma Sources Sci. Technol.* **28** 115015

[37] Vialetto L, Viegas P, Longo S and Diomede P 2020 *Plasma Sources Sci. Technol.* **29** 115006

[38] Viegas P, Vialetto L, van de Steeg A W, Wolf A J, Bongers W A, van Rooij G J, van de Sanden M C M, Diomede P and Peeters F J J 2021 *Plasma Sources Sci. Technol.* **30** 065022

[39] Babou Y, Rivière P, Perrin M-Y and Soufiani A 2008 *Plasma Sources Sci. Technol.* **17** 045010

[40] Janssen J F J 2016 Equilibrium and transport in molecular plasmas *PhD Thesis* Technische Universiteit Eindhoven

[41] Hassouni K, Leroy O, Farhat S and Gicquel A 1998 *Plasma Chem. Plasma Process.* **18** 325–62

[42] Baeva M, Hempel F, Baierl H, Trautvetter T, Foest R and Loffhagen D 2018 *J. Phys. D: Appl. Phys.* **51** 385202

[43] Fristrom R M and Monchick L 1988 *Combust. Flame* **71** 89–99

[44] Gleizes A, Gonzalez J J and Freton P 2005 *J. Phys. D: Appl. Phys.* **38** R153–83

[45] Hirschfelder J O and Curtiss C F 1948 Theory of propagation of flames. Part I: general equations *Symp. on Combustion and Flame, and Explosion Phenomena* vol 3 (Elsevier) pp 121–7

[46] Capitelli M, Bruno D and Laricchiuta A 2013 *Fundamental Aspects of Plasma Chemical Physics: Transport* vol 74 (New York: Springer)

[47] Laricchiuta A *et al* 2009 *Eur. Phys. J.* D **54** 607–12

[48] Mason E A, Munn R J and Smith F J 1967 *Phys. Fluids* **10** 1827–32

[49] Ramshaw J D 1993 *J. Non-Equil. Thermodyn.* **18** 121–34

[50] Kubečka M, Snirer M, Obrusník A, Kudrle V and Bonaventura Z 2020 *Plasma Sources Sci. Technol.* **29** 075001

[51] Somers B 1994 The simulation of flat flames with detailed and reduced chemical models *PhD Thesis* Technische Universiteit Eindhoven

[52] Giovangigli V 1990 *IMPACT Comput. Sci. Eng.* **2** 73–97

[53] Peerenboom K, van Boxtel J, Janssen J and van Dijk J 2014 *J. Phys. D: Appl. Phys.* **47** 425202

[54] Synek P, Obrusník A, Hübner S, Nijdam S and Zajíčková L 2015 *Plasma Sources Sci. Technol.* **24** 025030

[55] Yimer I, Campbell I and Jiang L-Y 2002 *Can. Aeronaut. Space J.* **48** 195–200

[56] Gist T E 1992 Multi-ion ambipolar diffusion *PhD Thesis* Air Force Institute of Technology, Faculty of the School of Engineering

[57] Mathur S, Tondon P K and Saxena S C 1967 *Mol. Phys.* **12** 569–79

[58] Wilke C R 1950 *J. Chem. Phys.* **18** 517–9

[59] McBride B J, Gordon S and Reno M 1993 Coefficients for calculating thermodynamic and transport properties of individual species vol 4513 (National Aeronautics and Space Administration: NASA Technical Memorandum)

[60] Gordon S, McBride B J and Zehe M J 2002 NASA Glenn coefficients for calculating thermodynamic properties of individual species *Technical Publication NASA/TP-2002-211556* (NASA Glenn)

[61] Aubrecht V and Bartlova M 2008 Radiation transfer in thermal plasmas of air, N_2 and CO_2 *2008 17th Int. Conf. on Gas Discharges and Their Applications* (IEEE) pp 393–6

[62] Moisan M and Nowakowska H 2018 *Plasma Sources Sci. Technol.* **27** 073001

[63] Hagelaar G J M, Hassouni K and Gicquel A 2004 *J. Appl. Phys.* **96** 1819–28

[64] Hagelaar G 2000 Modeling of microdischarges for display technology *PhD Thesis* Technische Universiteit Eindhoven

[65] Georgieva V *et al* 2017 *Plasma Process. Polym.* **14** 1600185

[66] Morillo-Candas A S 2019 Investigation of fundamental mechanisms of CO_2 plasmas *PhD Thesis* Ecole Polytechnique-Universitè Paris-Saclay

[67] Hassouni K, Silva F and Gicquel A 2010 *J. Phys. D: Appl. Phys.* **43** 153001

[68] LeVeque R J 2002 *Finite Volume Methods for Hyperbolic Problems* vol 31 (Cambridge: Cambridge University Press)

[69] Patankar S V 2018 *Numerical Heat Transfer and Fluid Flow* (Boca Raton, FL: CRC Press)

[70] Scharfetter D L and Gummel H K 1969 *IEEE Trans. Electron Devices* **16** 64–77

[71] Peerenboom K 2012 Modeling of magnetized expanding plasmas *PhD Thesis* Technische Universiteit Eindhoven

[72] Smith G P *et al* 2018 *GRI-MECH 3.0* http://combustion.berkeley.edu/gri-mech/version30/text30.html

[73] Scoggins J B 2017 Development of numerical methods and study of coupled flow, radiation, and ablation phenomena for atmospheric entry *PhD Thesis* Université Paris-Saclay and VKI

[74] Biagi database www.lxcat.net (retrieved on 17 December 2019)

[75] Itikawa database www.lxcat.net (retrieved on 17 December 2019)

[76] Cross sections extracted from Magboltz v11.10 http://magboltz.web.cern.ch/magboltz/ (accessed on 10 September 2020)

[77] IST-Lisbon database www.lxcat.net (retrieved on 31 July 2020)

[78] BSR database (quantum-mechanical calculations by O Zatsarinny and K Bartschat) www.lxcat.net (retrieved on 31 July 2020)
[79] Cenian A, Chernukho A, Borodin V and Śliwiński G 1994 *Contrib. Plasma Phys.* **34** 25–37
[80] Hokazono H and Fujimoto H 1987 *J. Appl. Phys.* **62** 1585–94
[81] Polak L S and Slovetsky D I 1976 *Int. J. Radiat. Phys. Chem.* **8** 257–82
[82] Annušová A, Marinov D, Booth J-P, Sirse N, da Silva M L, Lopez B and Guerra V 2018 *Plasma Sources Sci. Technol.* **27** 045006
[83] Kossyi I A, Kostinsky A Y, Matveyev A A and Silakov V P 1992 *Plasma Sources Sci. Technol.* **1** 207–20
[84] Morillo-Candas A S, Silva T, Klarenaar B L M, Grofulović M, Guerra V and Guaitella O 2020 *Plasma Sources Sci. Technol.* **29** 01LT01
[85] Berthelot A and Bogaerts A 2018 *J. CO_2 Util.* **24** 479–99
[86] Fowler R H 1924 *London, Edinburgh Dublin Phil. Mag. J. Sci.* **47** 257–77
[87] Ogloblina P, Tejero-del-Caz A, Guerra V and Alves L L 2020 *Plasma Sources Sci. Technol.* **29** 015002
[88] Vialetto L, Ben Moussa A, van Dijk J, Longo S, Diomede P, Guerra V and Alves L L 2021 *Plasma Sources Sci. Technol.* **30** 075001
[89] Laporta V, Cassidy C M, Tennyson J and Celiberto R 2012 *Plasma Sources Sci. Technol.* **21** 045005
[90] Cosby P C 1993 *J. Chem. Phys.* **98** 7804–18
[91] Laporta V, Celiberto R and Tennyson J 2013 *Plasma Sources Sci. Technol.* **22** 025001
[92] Albritton D L 1978 *At. Data Nucl. Data Tables* **22** 1–89
[93] Mcelroy D, Walsh C, Markwick A J, Cordiner M A, Smith K and Millar T J 2013 *Astron. Astrophys.* **550** A36
[94] Park C, Howe J T, Jaffe R L and Candler G V 1994 *J. Thermophys. Heat Transfer* **8** 9–23
[95] Gudmundsson J T and Thorsteinsson E G 2007 *Plasma Sources Sci. Technol.* **16** 399–412
[96] Park C 1989 A review of reaction rates in high temperature air *24th Thermophysics Conf.* pp 1–18
[97] Silva T, Britun N, Godfroid T and Snyders R 2014 *Plasma Sources Sci. Technol.* **23** 025009
[98] Carbone E A D, Hübner S, Palomares J M and van der Mullen J J A M 2012 *J. Phys. D: Appl. Phys.* **45** 345203
[99] Jimenez-Diaz M, Carbone E A D, van Dijk J and van der Mullen J J A M 2012 *J. Phys. D: Appl. Phys.* **45** 335204
[100] Hagelaar G J M 2015 *Plasma Sources Sci. Technol.* **25** 015015
[101] http://bolsig.laplace.univ-tlse.fr/ (accessed on 22 June 2021)
[102] Hagelaar G J M and Pitchford L C 2005 *Plasma Sources Sci. Technol.* **14** 722–33
[103] Groen P W C, Wolf A J, Righart T W H, van de Sanden M C M, Peeters F J J and Bongers W A 2019 *Plasma Sources Sci. Technol.* **28** 075016
[104] Zhong H, Shneider M N, Mokrov M S and Ju Y 2019 *J. Phys. D: Appl. Phys.* **52** 484001
[105] Zhong H, Shneider M N, Mao X and Ju Y 2021 *Plasma Sources Sci. Technol.* **30** 035002
[106] Fridman A and Kennedy L A 2004 *Plasma Physics and Engineering* (Boca Raton, FL: CRC Press)
[107] Popov N A 2009 *Plasma Phys. Rep.* **35** 436–49